39. Malmberg AB, Yaksh TL (1992) Antinociceptive actions of spinal nonsteroidal anti-inflammatory agents on the formalin test in the rat. J Pharmacol Exp Ther 263: 136 146.
40. Hunskaar S, Fasmer OB, Hole K (1985) Formalin test in mice, a useful technique for evaluating mild analgesics. J Neurosci Methods 14: 69–76.
41. Huttner WB, Schiebler W, Greengard P, De Camilli P (1983) Synapsin I (protein I), a nerve terminal-specific phosphoprotein. III. Its association with synaptic vesicles studied in a highly purified synaptic vesicle preparation. J Cell Biol 96: 1374–1388.
42. Balan L, Foltyn VN, Zehl M, Dumin E, Dikopoltsev E, et al. (2009) Feedback inactivation of D-serine synthesis by NMDA receptor-elicited translocation of serine racemase to the membrane. Proc Natl Acad Sci U S A 106: 7589–7594.
43. Lorenzo LE, Ramien M, St Louis M, De Koninck Y, Ribeiro-da-Silva A (2008) Postnatal changes in the Rexed lamination and markers of nociceptive afferents in the superficial dorsal horn of the rat. J Comp Neurol 508: 592–604.
44. Zylka MJ, Rice FL, Anderson DJ (2005) Topographically distinct epidermal nociceptive circuits revealed by axonal tracers targeted to Mrgprd. Neuron 45: 17–25.
45. Dubuisson D, Dennis SG (1977) The formalin test: a quantitative study of the analgesic effects of morphine, meperidine, and brain stem stimulation in rats and cats. Pain 4: 161–174.
46. Hunskaar S, Hole K (1987) The formalin test in mice: dissociation between inflammatory and non-inflammatory pain. Pain 30: 103–114.
47. Wheeler-Aceto H, Porreca F, Cowan A (1990) The rat paw formalin test: comparison of noxious agents. Pain 40: 229–238.
48. Merrill AW, Barter LS, Rudolph U, Eger EI 2nd, Antognini JF, et al. (2006) Propofol's effects on nociceptive behavior and spinal c-fos expression after intraplantar formalin injection in mice with a mutation in the gamma-aminobutyric acid-type(A) receptor beta3 subunit. Anesth Analg 103: 478–483.
49. Ghilardi JR, Svensson CI, Rogers SD, Yaksh TL, Mantyh PW (2004) Constitutive spinal cyclooxygenase-2 participates in the initiation of tissue injury-induced hyperalgesia. The J Neurosci 24: 2727–2732.
50. Harris JA (1998) Using c-fos as a neural marker of pain. Brain Res Bull 45: 1–8.
51. Gao YJ, Ji RR (2009) c-Fos and pERK, which is a better marker for neuronal activation and central sensitization after noxious stimulation and tissue injury? Open Pain 2: 11–17.
52. Ji RR, Befort K, Brenner GJ, Woolf CJ (2002) ERK MAP kinase activation in superficial spinal cord neurons induces prodynorphin and NK-1 upregulation and contributes to persistent inflammatory pain hypersensitivity. J Neurosci 22: 478–485.
53. Svensson CI, Tran TK, Fitzsimmons B, Yaksh TL, Hua XY (2006) Descending serotonergic facilitation of spinal ERK activation and pain behavior. FEBS Lett 580: 6629–6634.
54. Polgar E, Campbell AD, MacIntyre LM, Watanabe M, Todd AJ (2007) Phosphorylation of ERK in neurokinin 1 receptor-expressing neurons in laminae III and IV of the rat spinal dorsal horn following noxious stimulation. Mol Pain 3: 4.
55. Ji RR, Baba H, Brenner GJ, Woolf CJ (1999) Nociceptive-specific activation of ERK in spinal neurons contributes to pain hypersensitivity. Nat Neurosci 2: 1114–1119.
56. Dumin E, Bendikov I, Foltyn VN, Misumi Y, Ikehara Y, et al. (2006) Modulation of D-serine levels via ubiquitin-dependent proteasomal degradation of serine racemase. J Biol Chem 281: 20291–20302.
57. Mustafa AK, Kumar M, Selvakumar B, Ho GP, Ehmsen JT, et al. (2007) Nitric oxide S-nitrosylates serine racemase, mediating feedback inhibition of D-serine formation. Proc Natl Acad Sci U S A 104: 2950–2955.
58. Miyoshi Y, Hamase K, Okamura T, Konno R, Kasai N, et al. (2011) Simultaneous two-dimensional HPLC determination of free D-serine and D-alanine in the brain and periphery of mutant rats lacking D-amino-acid oxidase. J Chromatogr B Analyt Technol Biomed Life Sci 879: 3184–3189.
59. Panatier A, Theodosis DT, Mothet JP, Touquet B, Pollegioni L, et al. (2006) Glia-derived D-serine controls NMDA receptor activity and synaptic memory. Cell 125: 775–784.
60. Basu AC, Tsai GE, Ma CL, Ehmsen JT, Mustafa AK, et al. (2009) Targeted disruption of serine racemase affects glutamatergic neurotransmission and behavior. Mol Psychiatry 14: 719–727.
61. Labrie V, Fukumura R, Rastogi A, Fick LJ, Wang W, et al. (2009) Serine racemase is associated with schizophrenia susceptibility in humans and in a mouse model. Mol Genet 18: 3227–3243.
62. Wolosker H, Sheth KN, Takahashi M, Mothet JP, Brady RO Jr, et al. (1999) Purification of serine racemase: biosynthesis of the neuromodulator D-serine. Proc Natl Acad Sci U S A 96: 721–725.
63. Mori H, Inoue R (2010) Serine racemase knockout mice. Chem Biodivers 7: 1573–1578.
64. Sasabe J, Chiba T, Yamada M, Okamoto K, Nishimoto I, et al. (2007) D-serine is a key determinant of glutamate toxicity in amyotrophic lateral sclerosis. Embo J 26: 4149–4159.
65. Sandkuhler J (2007) Understanding LTP in pain pathways. Mol Pain 3: 9.
66. Fukuda T, Watanabe K, Hisano S, Toyooka H (2006) Licking and c-fos expression in the dorsal horn of the spinal cord after the formalin test. Anesth Analg 102: 811–814.
67. Fukuda T, Hisano S, Tanaka M (2009) Licking decreases phosphorylation of extracellular signal-regulated kinase in the dorsal horn of the spinal cord after a formalin test. Anesth Analg 109: 1318–1322.

Bioorganic & Medicinal Chemistry Letters 24 (2014) 3732–3735

Contents lists available at ScienceDirect

Bioorganic & Medicinal Chemistry Letters

journal homepage: www.elsevier.com/locate/bmcl

In silico and pharmacological screenings identify novel serine racemase inhibitors ☆

Hisashi Mori [a,b,c,*], Ryogo Wada [f], Jie Li [f], Tetsuya Ishimoto [c], Mineyuki Mizuguchi [a,b,c], Takayuki Obita [c], Hiroaki Gouda [d,e,*], Shuichi Hirono [d], Naoki Toyooka [a,b,f,*]

[a] Graduate School of Innovative Life Science, University of Toyama, Toyama 930-0194, Japan
[b] Graduate School of Innovative Life Science, University of Toyama, Toyama 930-8555, Japan
[c] Graduate School of Medicine and Pharmaceutical Sciences, University of Toyama, Toyama 930-0194, Japan
[d] School of Pharmacy, Kitasato University, Tokyo 108-8641, Japan
[e] School of Pharmacy, Showa University, Tokyo 142-8555, Japan
[f] Graduate School of Science and Technology for Research, University of Toyama, Toyama 930-8555, Japan

ARTICLE INFO

Article history:
Received 19 May 2014
Revised 25 June 2014
Accepted 1 July 2014
Available online 5 July 2014

Keywords:
Serine racemase inhibitors
NMDA receptor
In silico screening
D-Serine
Overactivation

ABSTRACT

D-Serine is a coagonist of the *N*-methyl-D-aspartate (NMDA)-type glutamate receptor and its biosynthesis is catalyzed by serine racemase (SR). The overactivation of the NMDA receptor has been implicated in the development of neurodegenerative diseases, strokes, and epileptic seizures, thus, the inhibitors of SR have potential against these pathological states. Here, we have developed novel inhibitors of SR by in silico screening and in vitro enzyme assay. The newly developed inhibitors have lower IC_{50} value comparing with that of malonate, one of the standard SR inhibitor. The structural features of novel inhibitors suggest the importance of central amide structure having a phenoxy substituent in their structure for the SR inhibitory activity. The present findings suggest the importance and rational development of new drugs for diseases of NMDAR overactivation.

D-Serine, a D-amino acid abundant in the mammalian brain, is an endogenous ligand of the glycine site of the NMDA receptor.[1] D-Serine is efficacious in potentiating the activity of the NMDA receptor[2,3] and its deletion was demonstrated to greatly decrease NMDA receptor activity.[4] D-Serine is synthesized by serine racemase (SR), an enzyme that directly converts L-serine into D-Serine.[5] To investigate the role of D-Serine in brain function, we have generated SR gene knockout (KO) mice with a 90% decrease in D-Serine level and demonstrated that NMDA-receptor-mediated neurodegeneration can be attenuated in SR-KO mice.[6,7] Furthermore, the deletion of SR gene in mice protected against experimental cerebral ischemia[8] and epileptic seizure.[9] Antagonists of the D-Serine binding site of the NMDA receptor are neuroprotective in models of stroke.[10] The involvement of D-Serine and SR in above pathophysiological conditions makes SR an excellent drug targets of overactivation of NMDAR.

Some SR inhibitors were reported, such as malonate,[11] di-peptides,[12] and some compounds identified in the high-throughput beads library screening.[13] However, rational approach to identify novel SR inhibitors with searching chemical database of existing compounds was not been reported. As the crystal structure of human SR (*h*SR) with its inhibitor malonate was reported,[14] we tried to identify potential compounds of *h*SR inhibitor with in silico screening, chemical synthesis, and in vitro enzyme assay. In these approaches, we developed novel *h*SR inhibitors and revealed important structural features of SR inhibitor.

We performed multi-filter virtual screening protocol to explore candidate compounds for novel *h*SR inhibitor, as shown in Figure 1. In the first stage of this protocol, the chemical database of Namiki Shoji Co. Ltd, which comprises approximately 4 million compounds, was subjected to the Tripos Topomer Search technology.[15–17] The Topomer Search is a 3D ligand-based virtual screening tool, which use one already-known inhibitor as a query molecule to search 'hit molecules' that exhibit similar three-dimensional shapes. The similarity between a query molecule and a molecule from chemical database is estimated by comparing pharmacophoric features and the shape similarity of the associated Topomers. This type of searching has been demonstrated to be effective for both 'lead hopping' and 'scaffold hopping', allowing us to identify *h*SR inhibitors with novel structure. Here, we selected one of dipeptide-like *h*SR inhibitors reported by Dixon et al.[13] (Supplementary Fig. 1) as a query molecule for our screening. This aimed to explore the chemical space that is different from one of malonate, which is a widely used *h*SR Inhibitor. By

☆ This paper is dedicated to the late Professor Hiroki Takahata for his outstanding contributions to nitrogen-containing heterocyclic chemistry.

* Corresponding authors.

http://dx.doi.org/10.1016/j.bmcl.2014.07.003
0960-894X/

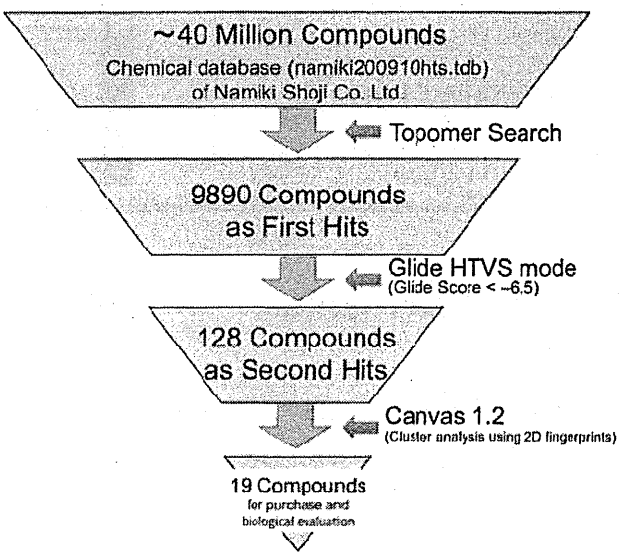

Figure 1. Multi-filter virtual screening.

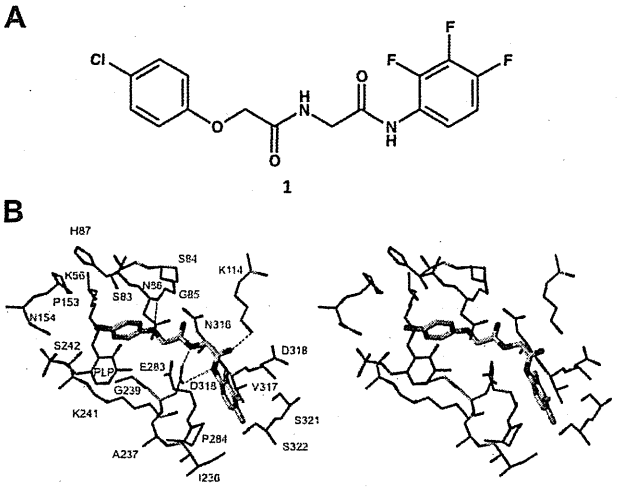

Figure 2. (A) Chemical structure of one of *h*SR inhibitors identified by our virtual screening protocol. (B) Stereoview of binding mode of **1** with *h*SR determined by our docking procedure. Hydrogen-bonding interactions are indicated by red dashed lines.

applying this first filter, we found 9890 chemical compounds as 'first hits'.

These 'first hits' were subsequently screened by high-throughput protein structure-based virtual molecular docking. In this molecular docking, we used the X-ray crystal structures of *h*SR in complex with malonate (PDB: 3L6B and 3L6R).[14] In addition, we prepared ligand-free form of *h*SR by homology modeling method, in which the X-ray crystal structure of ligand-free rat SR (*r*SR, PDB: 3HMK)[14] was used as a template. This modeling provided two structurally different ligand-free active sites of *h*SR, as the X-ray structure of ligand-free *r*SR was deposited as a dimer. As a result, a total of four active sites of *h*SR (two malonate-bound and two ligand-free forms) were used in this protein structure-based virtual screening. Docking was done with HTVS mode in GLIDE version 5.5 of Schrödinger Suite 2009. In order to determine the criteria value of GLIDE-HTVS-Score for this screening, we first docked five already-known *h*SR inhibitors,[13,18] of which inhibition constants (K_i) were reported (Supplementary Fig. 2). The resulting scores for these five inhibitors ranged from −10.44 to −4.92. We found that these GLIDE-HTVS-Scores were well correlated with RTln(K_i) for these five inhibitors (Supplementary Fig. 3), indicating that GLIDE-HTVS-Score is useful for extracting candidate compounds for *h*SR inhibitors. We set the criteria of GLIDE-HTVS-Score as −6.5, which is somewhat lower than that of the query molecule used in the first filter (−6.18). This was intended to search candidate compounds that may possess more potent inhibitory activities than the query molecule. In this second screening, we extracted 128 compounds as 'second hits'.

In order to reduce the number of virtual hits to purchase, the above second hits were finally clustered by similarity analysis based on 2D structural fingerprint.[19,20] This clustering was done with Canvas 1.2 of Schrödinger Suite 2009. As a result, we selected 19 compounds as the cluster representative, of which 18 compounds were commercially available and subjected to biological evaluation.

The identified 18 compounds were assayed with recombinant *h*SR with C2DC6D mutations[14] in vitro as described below. We could finally identify four small molecules with inhibitory activity against *h*SR from eighteen virtual hits, corresponding to a 'hit rate' of 22%. This high hit rate suggested that our multi-filter virtual screening protocol was quite useful for exploring novel *h*SR inhibitors. The chemical structure for one of these four compounds (**1**) is given in Figure 2A.[21] The IC_{50} value of **1** (1.21 mM) was comparable to that of malonate (1.31 mM) in our assay system (Fig. 3). To our knowledge, this is a first report of *h*SR inhibitor that possesses potent inhibitory activity comparable to malonate and a quite different structure from malonate analogs.

The interaction mode between **1** and *h*SR was examined by using a combination method of the molecular-docking calculation and the molecular mechanics Poisson–Boltzmann surface area (MM-PBSA) free energy analysis,[22] as detailed in the Supplementary data. In order to test our procedure, we first applied it to the malonate–*h*SR complex. The resulting model, that is the top-ranked pose, could reproduce all interactions between malonate and *h*SR observed in the crystal structure (Supplementary Fig. 4). The positional and conformational RMSDs relative to the X-ray pose were 0.58 and 0.20 Å, respectively. These results suggest that our procedure is appropriate for producing reliable interaction models of **1** and *h*SR. The resulting interaction model (the top-ranked pose) of **1** with *h*SR obtained by our procedure is shown in Figure 2B. The compound **1** was found to bind to the ligand-free form of *h*SR and form a total of four hydrogen bonds with N86, K114, and D238 of *h*SR. The 2,3,4-trifluorobenzene of **1** was located in the sub-pocket formed by I236, P284, V317, S321, and S322 of *h*SR to make hydrophobic interactions. The 4-chlorobenzene of **1** was found to make van der Waals interactions with PLP-K56, S83, S84, G85, N86, H87, P153, G239, and S242 of *h*SR, which were residues consisting of malonate-binding site in the crystal structure of malonate–*h*SR complex.

We tried to design some derivatives of **1** that were expected to be more potent for *h*SR. As shown in the left side of Figure 4, the chlorine atom of the 4-chlorobenzene of **1** was quite close to the hydroxyl group of S242 of *h*SR. This motivated us to consider the substitution of the chlorine atom by fluorine atom with stronger hydrogen-bond accepting ability, aiming at the formation of the additional hydrogen bond with S242. We could also consider the substitution of the chlorine atom by larger halogen atom such as bromine to increase the van der Waals or hydrophobic interactions with P153 of *h*SR. On the other hand, the surrounding of the 2,3,4-trifluorobenzene of **1** was indicated in the right side of Figure 4. The fluorine atoms of 2,3,4-trifluorobenzene of **1** seemed to be less important in the interaction of **1** with *h*SR, because they were exposed to solvents. Further, we could see that the hydrophobic side-chain of I236 of *h*SR was located in the neighborhood of the fluorine atom at position 4. Therefore, we considered the replacement of the 2,3,4-trifluorobenzene of **1** to a simpler mono-

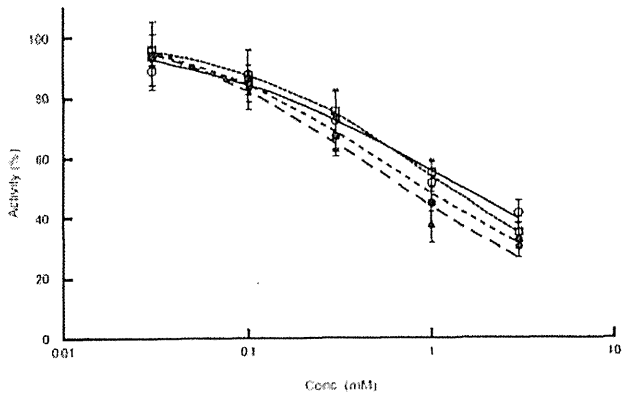

Figure 3. Dose–response curves of compounds inhibition against the hSR activity. Curves of malonate (○), Compounds **1** (□), **4i** (▲), and **4n** (●) are indicated.

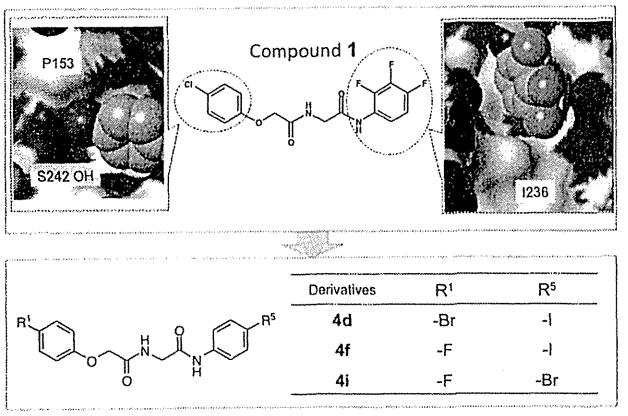

Figure 4. Molecular design of derivatives of **1**.

substituted benzene that has a larger halogen atom such as bromine or iodine at position 4, aiming at the increase of the van der Waals or hydrophobic interactions with I236 of *h*SR. This replacement was also expected to allow the synthesis of derivatives to be much easier.

Based on considerations described above, we designed three derivatives (**4d**, **4f**, and **4i**), as shown in the lower portion of Figure 4. The interaction mode of each derivative with *h*SR was predicted by the procedure we established in this study (see Supplementary Fig. 5). All derivatives retained the hydrogen-bonding interactions between **1** and *h*SR. As expected, the fluorine atoms introduced at R_1 of **4f** and **4i** were involved in the additional hydrogen-bonding interactions with S242 of *h*SR. The bromine and iodine atoms introduced at R_2 of **4d**, **4f**, and **4i** bromine made more closely contact with I236 of *h*SR than **1**.

The binding affinity of each derivative with *h*SR was approximated using a ligand efficiency (LE) index,[23] which was calculated by dividing the absolute value of ΔG_{bind} derived from MM-PBSA analysis by $N^{0.3}$, where N is the number of heavy atoms. As the LE index could decrease a ligand-size dependency of the interaction energy calculated by MM-PBSA method, it was known to be useful in the hit-to-lead optimization. The results are summarized in Table 1. For the demonstration of usefulness of LE indices, the calculation for the malonate–*h*SR complex is also included. The LE indices could give comparable values to both malonate and **1**, which is consistent with the experiment results showing that **1** possesses similar inhibitory activity to malonate. All derivatives of **4d**, **4f**, and **4i** showed greater LE indices than **1**, indicating that they might have better binding affinities. In the following section, the derivatives of **1** including **4d**, **4f**, and **4i** were synthesized and evaluated in vitro.

Table 1
Number of heavy atoms, binding free energies (ΔG_{bind}) calculated by MM-PBSA method, ligand efficiency (LE) indices, and experimental IC_{50}s for malonate, **1**, and derivatives **4d**, **4f**, and **4i**

Derivatives	Number of heavy atoms	ΔG_{bind} (kcal/mol)	LE[a] index	IC_{50} (mM)
Malonate	7	−14.58	8.13	1.31
1	25	−20.57	7.83	1.21
4d	23	−20.70	8.08	–[b]
4f	23	−20.35	7.94	–[b]
4i	23	−20.76	8.10	0.52

[a] LE index was calculated by dividing the absolute value of ΔG_{bind} derived from MM-PBSA method by $N^{0.3}$, where N is the number of heavy atoms.
[b] Not determined.

As a synthetic plan for derivatives of **1**, we divided the structure of **1** to two parts of building blocks **A** and **B**. The building block **A** is phenoxy-substituted acetic acid, and the building block **B** is Boc-protected glycine amide.

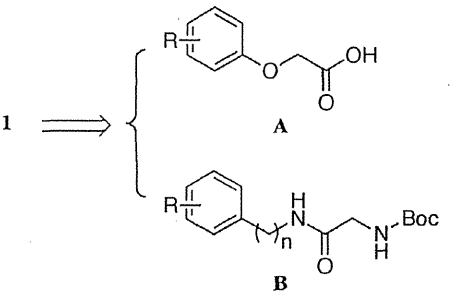

The Synthesis began with phenols (R^1 = Br or F, Scheme 1), which was converted to the corresponding ethers (**2a**:[24] R^1 = Br, **2c**:[25] R^1 = F, Scheme 1) by Williamson synthesis with methyl bromoacetate. Condensation of Boc-protected glycine with anilines (R^2 = I or Br, Scheme 1) using EDC provided the corresponding amides (**3b**:[26] R^2 = I, **3d**:[27] R^2 = Br, Scheme 1), which were converted to amines by deprotection of the Boc group with TFA. Condensation of amines, derived from **3b** and **3d**, with carboxylic acids, prepared by hydrolysis of **2a** and **2c** with LiOH, using CDI furnished the substituted acetamides (**4d**, **4f**, **4i**). To explore the more potent inhibitors, we synthesized further 33 compounds (see experimental details and Table 2 in the Supplementary material.)

Recombinant *h*SR with C2DC6D mutations and a His-tag to its carboxyl terminal was expressed in *Escherichia coli* and purified as described.[14] The purity of the used recombinant *h*SR was about 80%. The activity of the purified hSR (1 mM) in vitro was determined with 20 mM of L-serine and indicated concentration of compounds basically as described.[11,28] The inhibitory activity of new compounds was compared with that of malonate, one of the reported inhibitors.[11] We first screened the inhibitory activity of the compounds at 1 mM, and found that the compounds **4i** and **4n** showed higher inhibitory activity (Supplementary Table 2). Further dose–response analysis of the compounds detected that the **4i** showed significantly stronger inhibitory activity than that of malonate at 1 mM ($p = 0.005$, two-tailed student t test) and 3 mM ($p = 0.014$). The **4n** also showed significantly stronger inhibitory activity than that of malonate at 3 mM ($p = 0.035$). The IC_{50} values of the **4i** (0.52 mM) and the **4n** (0.63 mM) were lower than that of malonate (1.31 mM) (Fig. 3). Interestingly, compound **4i** with most potent inhibitory activity was one of three designed compounds based on the molecular-docking calculation and the free energy analysis. This result indicated that our procedure for molecular design of derivatives was quite useful.

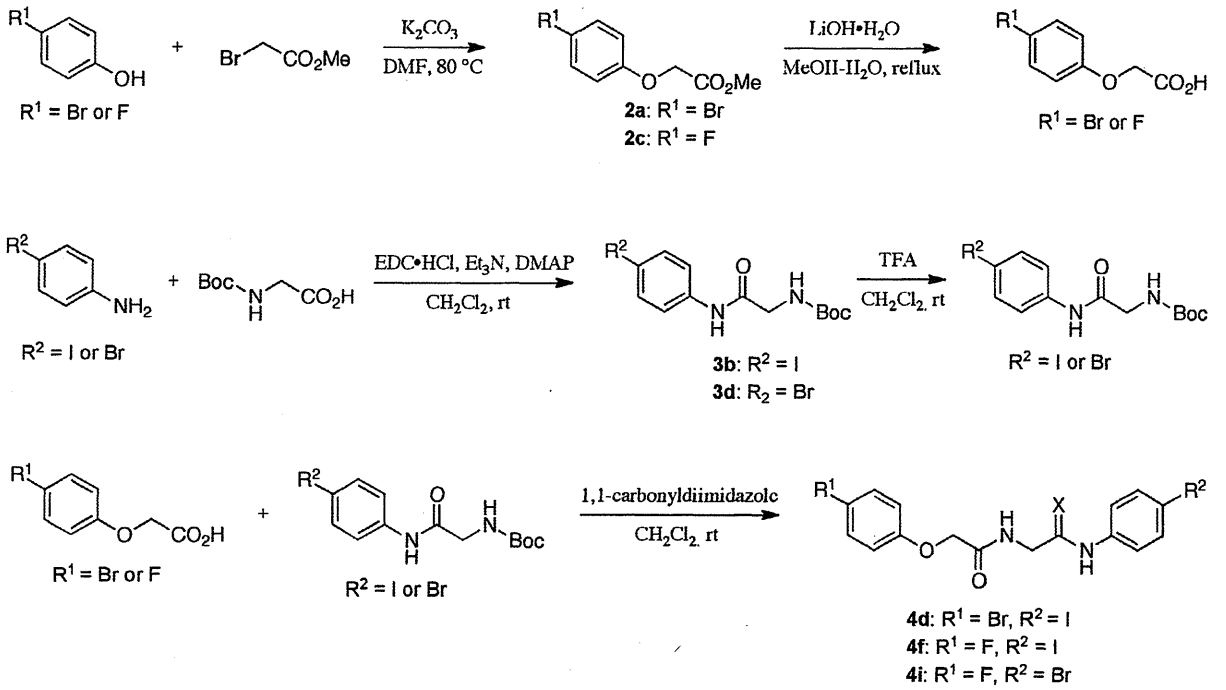

Scheme 1. Synthesis of derivatives **4d**, **4f**, **4i**.

The *p*-bromo substituent on the phenyl ring of the amide moiety in **4** was the best result (**4i** vs **4e**, **4f**, **4h**, **4k**, and **4w**). The *p*-bromo substituent on the phenyl ring of the ether moiety in **4** was also the best result (**4n** vs **4s**, **4t**, **4u**, **4v**, **4w**, **4y**, **4′**, and **4ii**). The conversion of the amide to thioamide (**4n** vs **4x**) was not effected for the inhibitory effect. The benzyl (**4i** vs **4p**, and **4n** vs **4z**, **4aa**, and **4bb**) or the cyclohexyl substituent (**4i** vs **4m**, and **4n** vs **4l**) instead of phenyl group on the amide moiety was also not affected.

In the present study, we identified the novel SR inhibitors with lower IC_{50} value comparing with that of malonate using in silico screening, chemical synthesis, binding modeling, and in vitro enzyme assay. Our approaches and obtained information of structural and predicted SR-novel chemicals interaction will be useful for further development of novel chemicals against neurodegenerative disorders with SR as a target.

Acknowledgments

We thank Riken NBRC and Prof. Yoshimura for providing the hSR cDNA clone and the Dsd1SC expression vector, respectively. This work was supported by Grants from Ministry of Education, Culture, Sports, Science, and Technology of Japan (Grant Nos. 221S0003 and 25293059 to H.M.) and the research fund of University of Toyama.

Supplementary data

Supplementary data (experimental details, Supplementary Figures 1–5, and Table 2 are included) associated with this article can be found, in the online version, at http://dx.doi.org/10.1016/j.bmcl.2014.07.003.

References and notes

1. Hashimoto, A.; Nishikawa, T.; Hayashi, T.; Fujii, N.; Harada, K.; Oka, T.; Takahashi, K. *FEBS Lett.* **1992**, *296*, 33.
2. Fadda, E.; Danysz, W.; Wroblewski, J. T.; Costa, E. *Neuropharmacology* **1988**, *27*, 1183.
3. Matsui, T.; Sekiguchi, M.; Hashimoto, A.; Tomita, U.; Nishikawa, T.; Wada, K. *J. Neurochem.* **1995**, *65*, 454.
4. Mothet, J. P.; Parent, A. T.; Wolosker, H.; Brady, R. O., Jr; Linden, D. J.; Ferris, C. D.; Rogawski, M. A.; Snyder, S. H. *Proc. Natl. Acad. Sci. U.S.A.* **2000**, *97*, 4926.
5. Wolosker, H.; Sheth, K. N.; Takahashi, M.; Mothet, J. P.; Brady, R. O., Jr.; Ferris, C. D.; Snyder, S. H. *Proc. Natl. Acad. Sci. U.S.A.* **1999**, *96*, 721.
6. Miya, K.; Inoue, R.; Takata, Y.; Abe, M.; Natsume, R.; Sakimura, K.; Hongou, K.; Miyawaki, T.; Mori, H. *J. Comp. Neurol.* **2008**, *510*, 641.
7. Inoue, R.; Hashimoto, K.; Harai, T.; Mori, H. *J. Neurosci.* **2008**, *28*, 14486.
8. Mustafa, A. K.; Ahmad, A. S.; Zeynalov, E.; Gazi, S. K.; Sikka, G.; Ehmsen, J. T.; Barrow, R. K.; Coyle, J. T.; Snyder, S. H.; Doré, S. *J. Neurosci.* **2010**, *30*, 1413.
9. Harai, T.; Inoue, R.; Fujita, Y.; Tanaka, A.; Horio, M.; Hashimoto, K.; Hongou, K.; Miyawaki, T.; Mori, H. *Epilepsy Res.* **2012**, *102*, 180.
10. Swanson, R. A.; Ying, W.; Kauppinen, T. M. *Curr. Mol. Med.* **2004**, *4*, 193.
11. Strísovský, K.; Jirásková, J.; Mikulová, A.; Rulísek, L.; Konvalinka, J. *Biochemistry* **2005**, *44*, 13091.
12. Kim, P. M.; Aizawa, H.; Kim, P. S.; Huang, A. S.; Wickramasinghe, S. R.; Kashani, A. H.; Barrow, R. K.; Huganir, R. L.; Ghosh, A.; Snyder, S. H. *Proc. Natl. Acad. Sci. U.S.A.* **2005**, *102*, 2105.
13. Dixon, S. M.; Li, P.; Liu, R.; Wolosker, H.; Lam, K. S.; Kurth, M. J.; Toney, M. D. *J. Med. Chem.* **2006**, *49*, 2388.
14. Smith, M. A.; Mack, V.; Ebneth, A.; Moraes, I.; Felicetti, B.; Wood, M.; Schonfeld, D.; Mather, O.; Cesura, A.; Barker, J. *J. Biol. Chem.* **2010**, *285*, 12873.
15. Cramer, R. D.; Poss, M. A.; Hermsmeier, M. A.; Caulfield, T. J.; Kowala, M. C.; Valentine, M. T. *J. Med. Chem.* **1999**, *42*, 3919.
16. Andrews, K. M.; Cramer, R. D. *J. Med. Chem.* **2000**, *43*, 1723.
17. Cramer, R. D.; Jilek, R. J.; Guessregen, S.; Clark, S. J.; Wendt, B.; Clark, R. D. *J. Med. Chem.* **2004**, *47*, 6777.
18. Hoffman, H. E.; Jirásková, J.; Ingr, M.; Zvelebil, M.; Konvalinka, J. *Protein Expr. Purif.* **2009**, *63*, 62.
19. Sastry, M.; Lowrie, J. F.; Dixon, S. L.; Sherman, W. *J. Chem. Inf. Model.* **2010**, *50*, 771.
20. Duan, J.; Dixon, S. L.; Lowrie, J. F.; Sherman, W. *J. Mol. Graph. Model.* **2010**, *29*, 157.
21. As other three compounds are now being pharmacologically characterized in our laboratory, the chemical structures will be shown after those are approved in international patent.
22. Kollman, P. A.; Massova, I.; Reyes, C.; Kuhn, B.; Huo, S.; Chong, L.; Lee, M.; Lee, T.; Duan, Y.; Wang, W.; Donini, O.; Cieplak, P.; Srinivasan, J.; Case, D. A.; Cheatham, T. E., 3rd. *Acc. Chem. Res.* **2000**, *33*, 889.
23. Nissink, J. W. *J. Chem. Inf. Model.* **2009**, *49*, 1617.
24. Abdel, M.; Hamid, E. S.; Ramadan, M.; Hagar, E. S.; El Ashry, H. *Synth. Commun.* **2004**, *34*, 377.
25. Soper, F.; Whitehead, C. W.; Behrens, O. K.; Corse, J. J.; Jones, R. G. *J. Am. Chem. Soc.* **1948**, *70*, 2849.
26. Annunziata, R.; Benaglia, M.; Puglisi, A.; Raimondi, L.; Cozzi, F. *Eur. J. Org. Chem.* **2008**, 3976.
27. Zhu, B.-Y.; Su, T.; Zhaozhong, J. J.; Scarborough, R. M.; Song, Y. PCT Int. Appl. 2000, WO 2000071507 A2 20001130.
28. Ito, T.; Takahashi, K.; Naka, T.; Hemmi, H.; Yoshimura, T. *Anal. Biochem.* **2007**, *371*, 167.

Journal of Molecular and Cellular Cardiology 72 (2014) 273–280

Contents lists available at ScienceDirect

Journal of Molecular and Cellular Cardiology

journal homepage: www.elsevier.com/locate/yjmcc

Original article

A590T mutation in KCNQ1 C-terminal helix D decreases I_{Ks} channel trafficking and function but not Yotiao interaction

Koshi Kinoshita [a,1], Takuto Komatsu [b,1], Kohki Nishide [b], Yukiko Hata [a], Nozomi Hisajima [b], Hiroyuki Takahashi [b], Katsuya Kimoto [b], Kei Aonuma [b], Eikichi Tsushima [b], Toshihide Tabata [b], Tomoyuki Yoshida [c], Hisashi Mori [c], Kunihiro Nishida [d], Yoshiaki Yamaguchi [d], Fukiko Ichida [e], Kenkichi Fukurotani [b], Hiroshi Inoue [d], Naoki Nishida [a,*]

[a] Department of Legal Medicine, Graduate School of Medical and Pharmaceutical Sciences, University of Toyama, 2630 Sugitani, Toyama, Toyama 930-0194, Japan
[b] Laboratory for Neural Information Technology, Graduate School of Sciences and Engineering, University of Toyama, 3190 Gofuku, Toyama, Toyama 930-8555, Japan
[c] Department of Molecular Neurosciences, Graduate School of Medical and Pharmaceutical Sciences, University of Toyama, 2630 Sugitani, Toyama, Toyama 930-0194, Japan
[d] Second Department of Internal Medicine, Graduate School of Medical and Pharmaceutical Sciences, University of Toyama, 2630 Sugitani, Toyama, Toyama 930-0194, Japan
[e] Department of Pediatrics, Graduate School of Medical and Pharmaceutical Sciences, University of Toyama, 2630 Sugitani, Toyama, Toyama 930-0194, Japan

ARTICLE INFO

Article history:
Received 1 November 2013
Received in revised form 28 February 2014
Accepted 26 March 2014
Available online 5 April 2014

Keywords:
$K_V7.1$
KCNQ1
KCNE1
I_{Ks}
LQT
Yotiao

ABSTRACT

KCNQ1 encodes the α subunit of the voltage-gated channel that mediates the cardiac slow delayed rectifier K^+ current (I_{Ks}). Here, we report a *KCNQ1* allele encoding an A590T mutation [KCNQ1(A590T)] found in a 39-year-old female with a mild QT prolongation. A590 is located in the C-terminal α helical region of KCNQ1 that mediates subunit tetramerization, membrane trafficking, and interaction with Yotiao. This interaction is known to be required for the proper modulation of I_{Ks} by cAMP. Since previous studies reported that mutations in the vicinity of A590 impair I_{Ks} channel surface expression and function, we examined whether and how the A590T mutation affects the I_{Ks} channel. Electrophysiological measurements in HEK-293T cells showed that the A590T mutation caused a reduction in I_{Ks} density and a right-shift of the current–voltage relation of channel activation. Immunocytochemical and immunoblot analyses showed the reduced cell surface expression of KCNQ1(A590T) subunit and its rescue by coexpression of the wild-type KCNQ1 [KCNQ1(WT)] subunit. Moreover, KCNQ1(A590T) subunit interacted with Yotiao and had a cAMP-responsiveness comparable to that of KCNQ1(WT) subunit. These findings indicate that the A590 of KCNQ1 subunit plays important roles in the maintenance of channel surface expression and function via a novel mechanism independent of interaction with Yotiao.

1. Introduction

KCNQ1 encodes the pore-forming α subunit of the voltage-gated K^+ channel KvLQT1 ($K_V7.1$) [1]. In cells of the atria and ventricles, KCNQ1 and the auxiliary subunit KCNE1 form a channel that mediates the slowly activating delayed rectifier outward K^+ currents I_{Ks}, which contributes to repolarization after the plateau phase of an action potential [2–4]. Mutations in the *KCNQ1* gene are thought to cause a subtype (LQT1) of long QT syndromes, which are inherited cardiac disorders characterized by a prolonged QT interval in the electrocardiogram (ECG) [5,6]. LQT1 patients are at risk of severe arrhythmic disorders such as torsades de pointes and sudden cardiac death, and constitute approximately 45% of congenital LQT syndrome cases [7].

The 300 amino acid residue C-terminal domain of KCNQ1 forms almost 50% of the entire subunit, and includes four helical regions, referred to as helices A–D (Fig. 1C) [8]. Helix A (residues 370–386) and helix B (residues 504–531) mediate binding of KCNQ1 with CaM, which is required for normal KCNQ1 channel gating, folding and membrane trafficking [9–11]. Helices C (residues 538–562) and D (residues 587–620), also termed the A-domain, Head and Tail, or TCC1 and TCC2, together form a tandem coiled-coil domain that is required for subunit-specific tetramerization and membrane trafficking [11,12]. Furthermore, helix D forms a I_{Ks} macromolecular signaling complex through an interaction with the anchoring protein Yotiao (also known as A-kinase anchoring protein 9: AKAP9) [13–15]. The modulation of channel activity supporting sympathetic regulation requires the cAMP-dependent recruitment by Yotiao of several key enzymes to the I_{Ks} complex, including PKA, PP1, PDE4D3, and AC9 [16,17]. The disruption of the cAMP-dependent I_{Ks} regulation by mutations in helix D indicates that Yotiao interacts with KCNQ1 through this domain [13].

* Corresponding author. Tel.: +81 76 434 7281; fax: +81 76 434 5024.
E-mail address: nishida@med.u-toyama.ac.jp (N. Nishida).
[1] K. Kinoshita and T. Komatsu contributed equally to this work.

http://dx.doi.org/10.1016/j.yjmcc.2014.03.019
0022-2828/

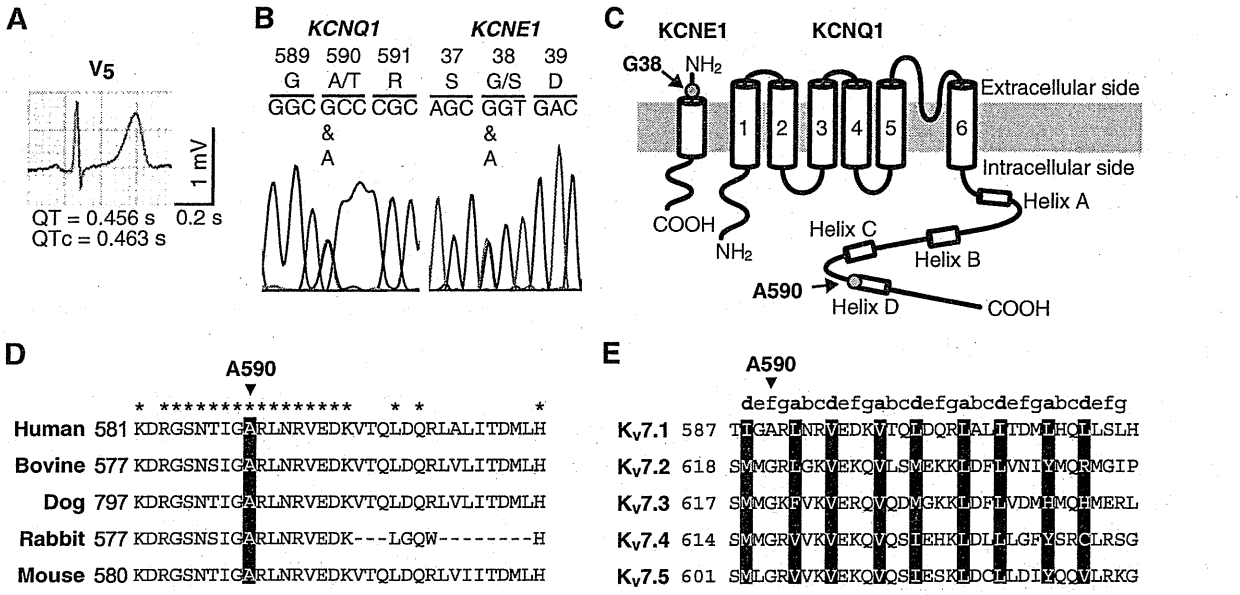

Fig. 1. Identification, sequence alignment, and structural model of KCNQ1(A590T). (A) ECG of the subject at rest. (B) Sequence analysis of *KCNQ1* (left) and *KCNE1* (right). Chromatograms indicate portions of the raw sequencing data of the subject's genomic DNA. Corresponding nucleotides and amino acids are shown above the chromatograms. Numbers denote the positions of the encoded amino acids. The heterozygous G to A transitions at position 1768 of *KCNQ1* and position 112 of *KCNE1* resulted in an alanine to threonine substitution at residue 590 (A590T), and a glycine to serine at residue 38 (G38S), respectively. (C) Schematic representation of KCNQ1 and KCNE1 subunits. Arrows denote the positions of the mutations. (D) Sequence homology among various mammals. Partial amino acid aligned at the position corresponding to A590 of human KCNQ1 (arrowhead). Numbers next to species indicate the position of the first amino acid of each partial sequence. Asterisk indicates the conserved amino acid among all of the orthologs. (E) Helix D sequences of human K_V7 family. The positions of the coiled-coil heptad repeats (abcdefg) are indicated above the sequence. The residues corresponding to the a and d positions of the heptad repeats are shaded.

Actually, several missense mutations causing LQTS have been identified in the vicinity of helix D [18–22]. Functional analyses have demonstrated that these KCNQ1 mutants, which include T587M [23–25], G589D [11,13,25–28], R591H [25,29], R594Q [25,30–32], and delV595 [33], are not functional, although they do not have a dominant-negative effect. Moreover, these mutants have impaired membrane trafficking, while they retain the ability to assemble into multimers [34].

In this study, we characterized a KCNQ1(A590T) mutation found in a 39-year-old female who had never experienced cardiac events. Although this mutation has previously been reported, its detailed functional analysis has not been performed to date [19,35,36]. Since A590 is located near the N-terminal end of helix D, where the previously reported LQT-associated mutations were located, we anticipated that the A590T mutation might affect the functional expression of I_{Ks}. To assess this possibility, we performed electrophysiological, biochemical and immunocytochemical analyses in a heterologous expression system of HEK-293T cell.

2. Materials and methods

2.1. Diagnosis and genetic analysis

Subject diagnosis and peripheral blood sampling was performed at the Second Department of Internal Medicine, Toyama University Hospital (Toyama, Japan) under the approval of the University's Committee on Utilization of Human Genes (#22-9). The protocol was performed in accordance to the Helsinki Declaration. Written informed consent was obtained from the subject before blood sampling. All exons of *KCNQ1*, *KCNH2*, *SCN5A*, *KCNE1*, and *KCNE2* were amplified from genomic DNA extracted from the blood sample. PCR products were analyzed by direct sequencing using an ABI PRISM 3100 genetic analyzer (Life Technologies, Carlsbad, CA, USA).

2.2. Plasmids

A pReceiver-M12 vector containing N-terminal 3× FLAG epitope and KCNQ1 cDNA (GenBank: AF000571) [FLAG-KCNQ1(WT)] was purchased from GeneCopoeia (Rockville, MD, USA). FLAG-KCNQ1(A590T) or FLAG-KCNQ1(G589D) was generated by site-directed mutagenesis of FLAG-KCNQ1(WT). KCNE1 cDNA (GenBank: AF135188) was cloned from genomic DNA in adult human peripheral blood and inserted into the pReceiver-M12 vector. Yotiao cDNA (GenBank: NM_147166) was synthesized from the commercially available total RNA of human adult cardiomyocyte (BD Biosciences, San Jose, CA, USA) using SuperScript III (Life Technologies) and inserted into pReceiver-M12 vector using an In-Fusion HD cloning Kit (Takara, Kyoto, Japan). The Myc- or HA-tagged plasmid vectors were constructed by replacing the 3× FLAG sequence of the pReceiver-M12 vector with an oligo DNA containing 2× Myc (GGGGSASMQKLISEEDL) or 2× HA (GGGGSYPYDVPDYA) sequences, respectively. The V5 (GKPIPNPLLGLDST) or HA (GSYPYDVPDYAG) sequence was inserted into the extracellular S1–S2 loop of FLAG- or Myc-KCNQ1 after nucleotide position 438 between E146 and Q147 (pCAGGS-$V5_{ins}$-KCNQ1, FLAG-HA_{ins}-KCNQ1(WT), or Myc-HA_{ins}-KCNQ1(A590T), respectively).

2.3. Cell culture and transient transfection

HEK-293T cells were cultured in DMEM (Life Technologies) supplemented with 10% FBS at 37 °C in 5% CO_2. Vectors were transiently transfected using TransIT-293 reagent (Mirus Bio, Madison, WI, USA) according to the manufacturer's instructions. For electrophysiological experiments, pCAGGS-EGFP, FLAG-KCNE1, and either FLAG-KCNQ1(WT), FLAG-KCNQ1(A590T) or a 1:1 mixture of these vectors were transfected at a ratio of 1:4.5:4.5. For immunocytochemistry, pCAGGS-KCNE1 and either pCAGGS-$V5_{ins}$-KCNQ1(WT), pCAGGS-$V5_{ins}$-KCNQ1(A590T), or a

1:1 mixture of pCAGGS-KCNQ1(WT) and pCAGGS-$V5_{ins}$-KCNQ1(A590T) were transfected at a ratio of 1:1. For immunoblotting of the extracellular labeled proteins, FLAG-HA_{ins}-KCNQ1(WT), Myc-HA_{ins}-KCNQ1(A590T), or a 1:1 mixture of these vectors was transfected. For immunoprecipitation experiments, FLAG-Yotiao, HA-KCNE1, and either Myc-KCNQ1(WT), Myc-KCNQ1(A590T), Myc-KCNQ1(G589D) or a 1:1 mixture of Myc-KCNQ1(WT) and Myc-KCNQ1(A590T) were transfected at a ratio of 4:1:1. For cAMP response experiments, pCAGGS-EGFP, FLAG-Yotiao, FLAG-KCNE1, and either FLAG-KCNQ1(WT) or FLAG-KCNQ1(A590T) were transfected at a ratio of 0.5:4:1:1.

2.4. Electrophysiology

Rupture-patch whole-cell voltage-clamp recordings were carried out in EGFP-positive cells. Cells were perfused continuously with a warmed-bath solution (36–38 °C). Current signals were acquired with an EPC 8 amplifier controlled by PatchMaster software (HEKA, Lambrecht, Germany). A glass recording pipette filled with (in mM) 134 potassium D-gluconic acid, 7.6 KCl, 9 KOH, 10 NaCl, 1.2 $MgCl_2$, 10 HEPES, 0.5 EGTA, and 4 adenosine triphosphate magnesium salt (pH 7.3 with KOH) was used and had a tip resistance of 3–5 MΩ. To measure the effect of cAMP-responsiveness of the current, 300 μM 8-CPT-cAMP (Abcam) and 0.2 μM Okadaic acid (Millipore) were added to a pipette solution filled with (in mM) 110 K-aspartate, 1 $CaCl_2$, 1 $MgCl_2$, 10 HEPES, 11 EGTA, and 5 mM adenosine triphosphate potassium salt (pH 7.3 with KOH). Normal Tyrode's solution was used for the bath solution.

2.5. Immunocytochemistry

For labeling the S1–S2 extra loop of the KCNQ1, cells were incubated with anti-V5 antibody (1:1000) in DMEM containing 10% FBS (37 °C, 5% CO_2, 1 h). Cells were fixed with 4% paraformaldehyde (RT, 20 min), followed by blocking with 10% donkey serum (RT, 30 min). To detect the KCNQ1 proteins, cells were incubated with Alexa Fluor 488-conjugated donkey anti-mouse antibody (1:500) (RT, 1 h). Immunofluorescence was captured using a TCS-SP5 confocal microscope (Leica).

2.6. Coimmunoprecipitation and immunoblotting

48 h after transfection, cells were incubated with anti-HA antibody (1:500, Y-11; Santa Cruz Biotechnology, Inc.) in DMEM containing 10% FBS (37 °C, 5% CO_2, 1 h). To prepare the whole cell lysates, cells were lysed with 150 μl of the buffer containing 150 mM NaCl, 20 mM Tris-HCl (pH 7.5), 0.5 mM EDTA, 0.25% Triton-X-100, and protease inhibitor on ice for 30 min. After the centrifugation (15,000 rpm, 20 min), whole cell lysates were treated with 20 μl of Dynabeads Protein G (Life Technologies) in a rotator at RT for 1 h. The antibody–protein complex bound to the beads was extracted by incubation with SDS sample buffer at RT for 30 min. N-terminal FLAG- or Myc-tagged proteins were detected using monoclonal HRP-conjugated anti-epitope tag antibodies (MBL, Nagoya, Japan). HA-tagged proteins were detected with a mouse monoclonal anti-HA antibody (Roche) and a HRP-conjugated anti-mouse antibody (GE Healthcare). Calnexin was detected with a rabbit polyclonal anti-calnexin antibody (Cell Signaling Technology) and a HRP-conjugated anti-rabbit antibody (GE Healthcare).

2.7. Statistics

Each numerical data group is expressed as mean ± SEM except otherwise stated. When the majority of the groups had normal distributions ($p \geq 0.05$, Shapiro–Wilk test), an unpaired *t*-test was used to examine statistical differences; otherwise, the Wilcoxon rank sum test was used.

3. Results

3.1. Clinical phenotype, genotype, and subunit structure

A 39-year-old Japanese female was referred to the Second Department of Internal Medicine, Toyama University Hospital because her two sons showed mild QT interval prolongations [Bazett-corrected QT interval (QTc), 448 ms and 454 ms for the 15- and 12-year-old sons, respectively] in their ECGs at a school physical examination. She also showed a mild QT prolongation (QTc, 463 ms; Fig. 1A). All the members of this family have been asymptomatic and had no history of cardiac problems. Sequence analysis of the LQTS-related genes showed that the mother carried heterozygous mutations in *KCNQ1* and *KCNE1* genes, causing A590T and G38S substitutions in KCNQ1 and KCNE1 subunits, respectively (Fig. 1B). Since functional analysis of the G38S mutation has been described in previous studies [37,38], we focused on the A590T mutation. No mutation was identified in any other major LQTS-related genes, including *KCNH2*, *SCN5A* and *KCNE2* (data not shown).

A590 of KCNQ1 is located at the N-terminal end of helix D (Fig. 1C) and is conserved among mammalian KCNQ1 orthologs (Fig. 1D), whereas other members of the human K_V7 family contain a glycine at the corresponding position (Fig. 1E). The helix D contains heptad repeats $(abcdefg)_n$, which are suggested to play an important role in subunit assembly. A590T is out of the key positions of the heptad repeat (a and d) and is suggested not to face the inter-subunit interface, implying that the A590T mutation might not severely affect subunit assembly [11,25,39,40].

3.2. Effects of A590T mutation on I_{Ks} basic properties

To analyze the functional characteristics of KCNQ1(A590T) subunit, we compared currents in cells transfected with KCNE1 and either KCNQ1(WT), KCNQ1(A590T), or a 1:1 mixture of KCNQ1(WT) and KCNQ1(A590T) (WT, AT, and WT/AT cells, respectively) under voltage clamp. We applied a double-voltage-step stimulus, consisting of an initial voltage step with a varying voltage (V_{first}) and a subsequent voltage step of −50 mV. We confirmed that non-transfected cells and cells transfected with KCNQ1 alone did not have large tail currents as seen in the above cells, suggesting that co-expressed KCNE1 indeed affected KCNQ1 and augmented I_{Ks} (Supplemental Fig. 1). In addition, the activation rate of I_{Ks} recorded at a temperature of 37 °C (Fig. 2) was faster than that at a temperature of 25 °C (Supplemental Fig. 2).

The amplitude of the depolarization-evoked currents in the AT cells was smaller than those in the WT and WT/AT cells (Fig. 2A). We used the peak density of the tail current (I_{tail}) to quantify the absolute amplitude and the activation extent of I_{Ks} (Fig. 2B). The I_{tail} density was significantly smaller in the AT cells than in the WT cells with V_{first} from −40 to 10 mV (Fig. 2B). In contrast, the I_{tail} density did not differ between the WT/AT and WT cells for any tested V_{first}. The V_{50} and slope factor were estimated from the Boltzmann equation fitted to the I_{tail} density–V_{first} plot (Fig. 2C). The V_{50} of the AT cells was more positive by 10.2 mV than that of the WT cells, whereas no difference in the V_{50} was detected between the WT/AT and WT cells (Fig. 2D). The slope factor did not differ among all the cell groups (Fig. 2E). In addition, we assessed the effect of the double mutations KCNQ1(A590T) and KCNE1(G38S) which mimicked the molecular environment of the subject (Fig. 1B, C). Cells expressing both the mutant subunits had a significantly smaller I_{Ks} than cells expressing KCNQ1(A590T) and KCNE1(WT) (from −10 to 40 mV, Supplemental Figs. 3A–C). The activation rate, V_{50}, and slope factor were not significantly different between these cell groups (Supplemental Figs. 3D, E).

3.3. Reduced cell surface expression of KCNQ1(A590T) subunit and its rescue by KCNQ1(WT) subunit

Next, we examined the cell surface expression of KCNQ1(A590T) because the mutations in the vicinity of A590 were known to impair the

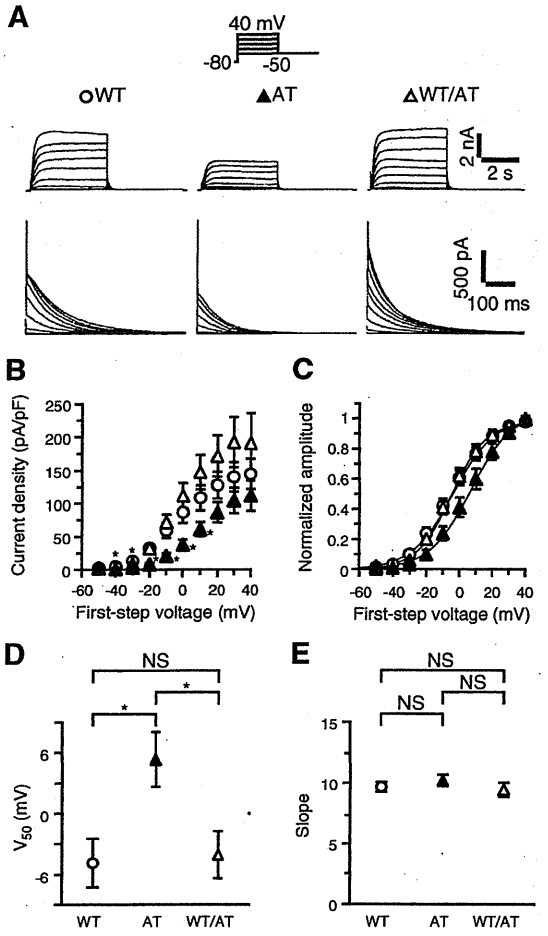

Fig. 2. Effects of the A590T mutation on I_{Ks}. (A) Ionic currents evoked by 4 s depolarizing pulses of voltages (V_{first}, −50 to 40 mV) followed by a 4 s repolarizing pulse (−50 mV). Representative current traces from WT, AT, and WT/AT cells. Lower traces are the close-ups of the I_{tail}. (B) Current–voltage relations of the peak tail current density. The means of WT (N = 19–25 for each point), AT (N = 16–17 for each point), and WT/AT (N = 15–22 for each point) cells are shown as open circles, filled triangles, and open triangles, respectively. With a V_{first} of 0 mV, the current densities were 84 ± 15.9 pA/pF, 38 ± 7.2 pA/pF, and 111 ± 19.0 pA/pF for the WT, AT, and WT/AT cells, respectively. *p < 0.05 vs. the WT cells, Wilcoxon rank sum test. (C) Normalized current–voltage relations. The data were taken from the same cells as in panel B. To depict these plots, the data were maximum-normalized for each cell and then averaged, and maximum-normalized over the cell group. Smooth curves indicate the Boltzmann functions fitted to the collection of all the adopted data. (D) Mean V_{50} estimated from the Boltzmann functions fitted to the current–voltage relations of the individual cells. WT: −4.87 ± 2.5 mV, AT: 5.33 ± 2.7 mV, WT/AT: −4.05 ± 2.3 mV. *p < 0.05, unpaired *t*-test. NS, p ≥ 0.05. (E) Mean slope factor estimated from the fitted Boltzmann functions. WT: 9.71 ± 0.41, AT: 10.2 ± 0.46, WT/AT: 9.45 ± 0.57. NS, p ≥ 0.05, Wilcoxon rank sum test.

membrane trafficking of the subunit. In this experiment, we used the V5 or HA tag-inserted KCNQ1 constructs to label the S1–S2 loop, which is located on the extracellular side of the subunit. We performed immunofluorescent labeling without permeabilization so that only the KCNQ1 proteins expressed on the cell surface were stained. The fluorescence signal of KCNQ1(A590T) subunit was detected while its intensity was lower than that of KCNQ1(WT) subunit (Fig. 3A). On the other hand, the fluorescence signal of KCNQ1(A590T) subunit increased when co-expressed with WT subunit.

To quantify the cell surface expression level, we performed densitometry on the immunoblots of the whole cell extracts (Input) and the surface-expressed proteins that were isolated as anti-HA antibody-bound fractions (Beads, Fig. 3B–D). The relative density of the surface-expressed KCNQ1(A590T) subunit (16.8 ± 4.3%, Input was taken as 100%) was lower than that of the surface-expressed KCNQ1(WT) subunit (46.4 ± 6.8%) (Fig. 3B). Next, we examined the cell surface expression level of KCNQ1(WT) or KCNQ1(A590T) subunits individually when co-expressed with both (WT/AT cells). FLAG-HA_{ins}-KCNQ1(WT) or Myc-HA_{ins}-KCNQ1(A590T) subunits (WT or AT cells) were detected by FLAG- or Myc-antibody, respectively (Fig. 3C, D). The relative density of the surface-expressed KCNQ1(WT) subunits in the WT/AT cells was similar to that of the WT cells (Fig. 3C). However, the relative density of the surface expressed KCNQ1(A590T) subunits in the WT/AT cells was 1.66-fold higher than that of the AT cells (Fig. 3D). These results indicate that the impaired membrane trafficking of the KCNQ1(A590T) subunit was rescued by the co-expression with KCNQ1(WT) subunit.

3.4. Effect of A590T mutation on interaction of KCNQ1 with KCNE1 and Yotiao

The helix D region of KCNQ1 subunit contains G589, the amino acid that has been suggested to be important for interaction between KCNQ1 and Yotiao and the cAMP-dependent modulation of I_{Ks} [13]. We examined whether the A590T mutation affects physical interaction between these proteins. Proteins derived from cells transfected with KCNE1, Yotiao, and either KCNQ1(WT), KCNQ1(A590T), or KCNQ1(G589D) were co-immunoprecipitated using an anti-KCNQ1 antibody. KCNQ1, Yotiao and KCNE1 were detected in the anti-KCNQ1 immunoprecipitates from all the cell groups, suggesting that the KCNQ1(A590T) or KCNQ1(G589D) mutation did not disrupt the KCNQ1–KCNE1–Yotiao interaction (Fig. 4).

3.5. Effect of A590T mutation on cAMP-dependent I_{Ks} modulation

Next, we examined whether the A590T mutation affects the cAMP-dependent modulation of I_{Ks} by monitoring I_{Ks} during an intracellular dialysis with a pipette solution containing the control vehicle or CPT-8-cAMP and Okadaic acid (cAMP/OA), which mimicked sympathetic stimulation [13]. We applied 60 mV depolarization steps with a 1 min interval to cells transfected with KCNE1, Yotiao, and either KCNQ1(WT) or KCNQ1(A590T) (WT and AT cells, respectively) (Fig. 5A). The effect of the dialysis was evaluated by the increase of peak I_{tail} amplitude from 1 min to 10 min of membrane rupture. The control pipette solution increased the I_{tail} of WT and AT cells by 22.7 ± 6.1% and 12.3 ± 4.8% for the WT and AT cells, respectively (Fig. 5B). cAMP/OA had significantly greater effects on the I_{tail} of both cell groups (43.2 ± 6.9% and 29.9 ± 5.8% for WT and AT cells, respectively; Fig. 5C, Supplemental Fig. 4C). We further examined the effect of the intracellular dialysis with cAMP/OA on the voltage-dependence of I_{Ks} by comparing the I_{tail}–V_{first} relations at 0 min and 5 min of membrane rupture (Fig. 6A, B). In both the WT and AT cells, the intracellular dialysis left-shifted the I_{tail}–V_{first} relations with a change in V_{50} (from −5.84 ± 1.48 to −18.62 ± 2.52 mV and from −6.69 ± 3.13 to −16.24 ± 2.74 mV, respectively). These results indicate that the A590T mutation does not affect the cAMP-dependent I_{Ks} modulation.

In addition, we examined the cAMP-responsiveness of I_{Ks} in KCNQ1(G589D)-expressed cells (GD cells). The GD cells showed only small I_{Ks} currents; the I_{tail} characteristic of I_{Ks} was detectable but the current seen at the first voltage step was indistinguishable from the native currents (Supplemental Figs. 4A, B, cf. Supplemental Fig. 1A, non-transfected cell). The markedly reduced amplitude of I_{Ks} with the G589D mutation has been reported previously [11,13,25,26]. We found that in the GD cells, the I_{tail} increased in response to the intracellular dialysis with cAMP/OA (Supplemental Figs. 4A–C). The extent of the increase appeared to be greater for the GD cells than for the WT and AT cells (albeit previous studies report the cAMP-insensitivity of KCNQ1(G589D)-mediated I_{Ks} [13,28]).

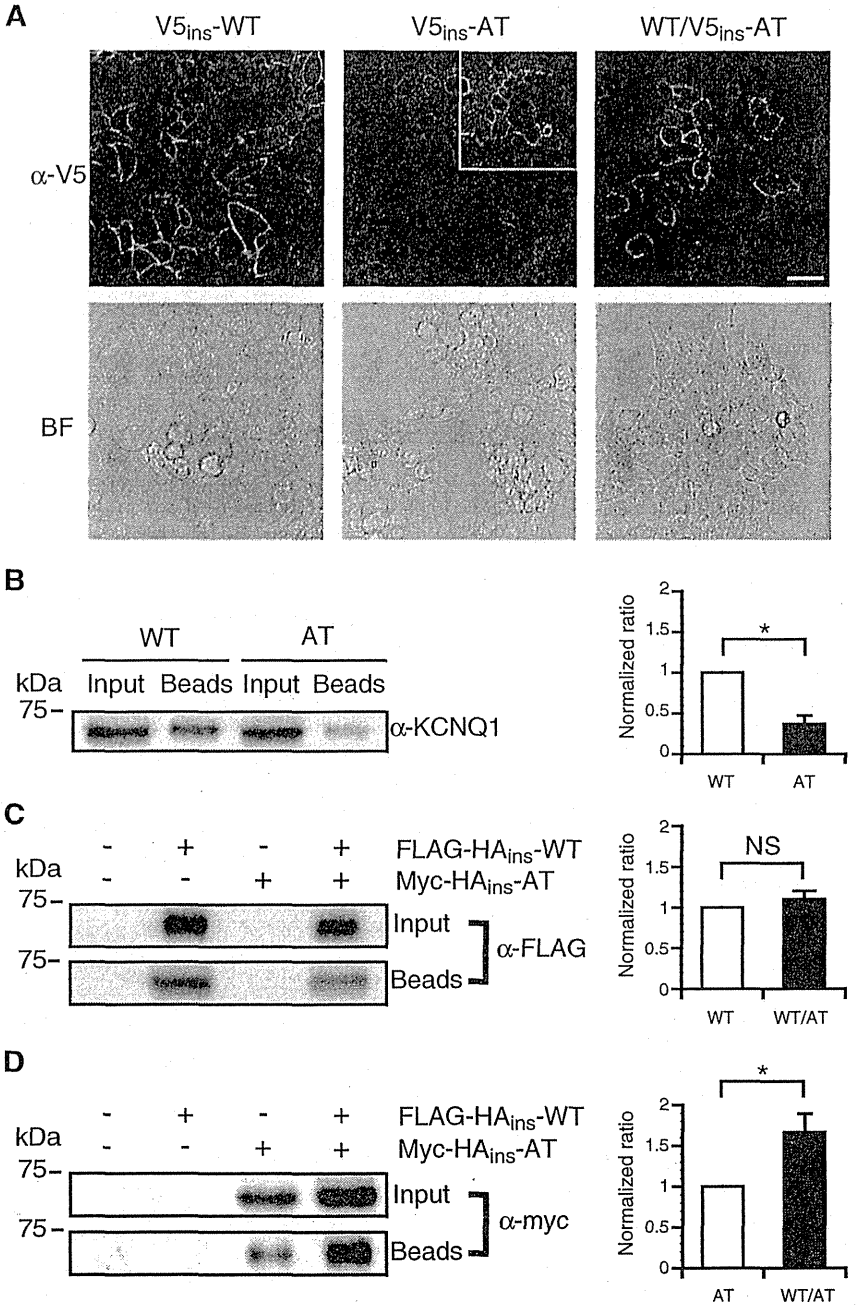

Fig. 3. The analysis of cell surface expression level of the KCNQ1(A590T) subunit. (A) Laser confocal images of HEK-293T cells transfected with KCNE1 and either $V5_{ins}$-KCNQ1(WT), $V5_{ins}$-KCNQ1(A590T) or a 1:1 mixture of KCNQ1(WT) and $V5_{ins}$-KCNQ1(A590T) (WT, AT, or WT/AT, respectively). The KCNQ1 protein expressed at the cell surface were immunolabeled using anti-V5 antibody and Alexa Fluor 488 antibody without permeabilization. All the images were acquired using PMT detector with smart gain of 600 V except the right top area of AT cells which was acquired by 700 V. Scale bars, 50 μm. BF, Bright field. (B) The ratio of the bead-bound fraction (KCNQ1 proteins expressed at the cell surface) contained in the input was examined by immunoblotting using anti-KCNQ1 antibody. *Left*, FLAG-HA_{ins}-KCNQ1(WT) or FLAG-HA_{ins}-KCNQ1(A590T) was transfected into the cells (WT or AT, respectively). *Right*, comparison of the density of the bead-bound fraction. For each of the labeled cell group, the density was normalized to the value of input. Bar and error bar, mean ± SD. $^{*}p < 0.05$, Wilcoxon rank sum test, N = 3 for each cell group. (C, D) *Left*, the immunoblots detecting the KCNQ1(WT) or KCNQ1(A590T) expressed at the cell surface using anti-FLAG or -Myc antibodies, respectively. 375 ng of FLAG-HA_{ins}-KCNQ1(WT), 375 ng of Myc-HA_{ins}-KCNQ1(A590T), or both (total 750 ng) were transfected into the cells (WT, AT, or WT/AT, respectively). HA-inserted KCNQ1 proteins were labeled with an anti-HA antibody before the harvest and then the antibody-bound fractions were isolated using Dynabeads. The bands were the predicted monomers of the KCNQ1 subunits. *Right*, densitometry of cell surface expression levels. The level is scored as the ratio of the density of the bead-bound fraction to that of the Input (Beads/Input). Signals were normalized to the value of homozygous expression of WT or AT, and expressed as ratio. NS, $P \geq 0.05$, Wilcoxon test. N = 3 for each cell group.

4. Discussion

In this study, we performed functional analyses on KCNQ1 with an A590T mutation at the N-terminal side of helix D (Fig. 1C). In the vicinity of A590, several LQT-related mutations have been identified such as the T587M, G589D, R591H, and R594Q mutations. Helices A–D in the C-terminal tail (residues 352–676) of human KCNQ1 have been suggested to play important roles in the maintenance of normal I_{Ks} function

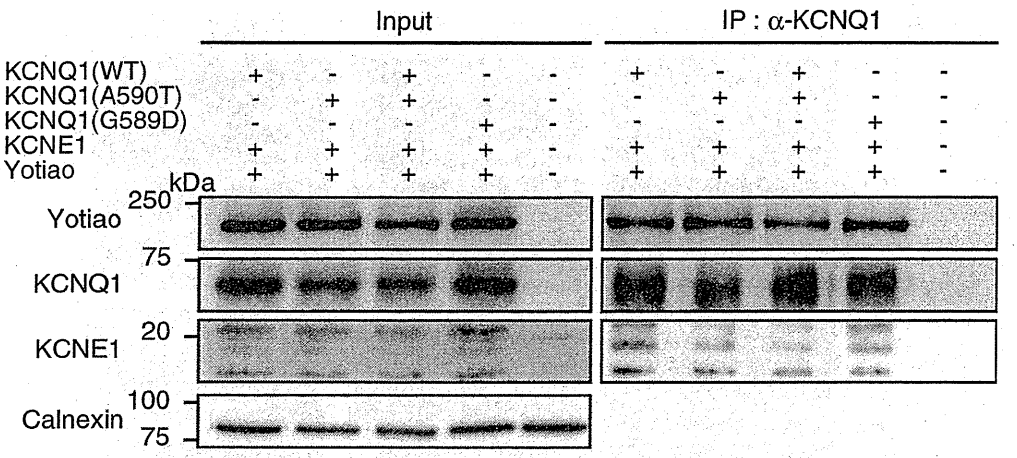

Fig. 4. KCNQ1 mutant subunits interact with KCNE1 subunit and Yotiao. Whole cell extracts (Input) of the cells transfected with FLAG-Yotiao, Myc-KCNQ1 and HA-KCNE1 were prepared and immune complexes were precipitated with an anti-KCNQ1 polyclonal antibody and Dynabeads. Yotiao, KCNQ1 and KCNE1 were detected with anti-FLAG, anti-Myc, and anti-HA antibodies, respectively. As a control, a rabbit monoclonal anti-calnexin antibody was used for detecting the protein levels of the inputs.

by regulating subunit folding and assembly, channel trafficking and gating. Our functional analyses of KCNQ1(A590T) subunit-containing channels may further clarify the structure–function relations of these helices.

We found that the A590T mutation attenuated the amplitude of I_{Ks} (Fig. 2A, B) and decreased cell surface expression (Fig. 3). The previously reported mutations in the vicinity of A590 also exerted similar effects on I_{Ks} amplitude and membrane trafficking. As compared with the reported mutations, the A590T mutation caused mild reduction in I_{Ks} amplitude (Fig. 2A, B) and cell surface expression (Fig. 3) [23–26,29,31]. This suggests that the severity of I_{Ks} function impairment reflects the severity of the decreased cell surface expression level. The fact that these effects are commonly seen in reported mutations suggests that the N-terminal side of helix D is important for membrane trafficking and that amino acid changes in this region impair the I_{Ks} channel function dependent on the cell surface expression level. We also found that the A590T mutation decreases the voltage-sensitivity of I_{Ks} (i.e., a right-shift of the I–V relation; Fig. 2C). The G589D mutation has been reported to have a similar effect on the voltage-sensitivity [26]. This suggests that the N-terminal side of helix D is also important for determining the voltage-dependence of channel activation.

The cells co-expressing KCNQ1(A590T) and KCNQ1(WT) subunit had I_{Ks} with a comparable amplitude to that of the cells expressing

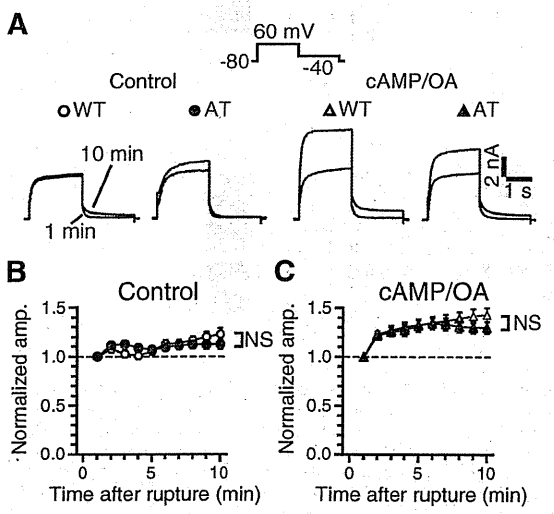

Fig. 5. Comparison of cAMP-dependent modulation of KCNQ1(WT) and KCNQ1(A590T). (A) Augmentation of I_{Ks} in response to the intracellular perfusion with the pipette solution without (control) or with 300 μM 8-CPT-cAMP and 0.2 μM Okadaic acid (cAMP/OA). The cells were transfected with EGFP, KCNE1, Yotiao and either KCNQ1(WT) or KCNQ1(A590T) (WT or AT cells, respectively). The currents evoked by a double-voltage-step stimulus (schematic above representative traces) were measured repetitively with an interval of 1 min. Representative current traces acquired at 1 min and 10 min were shown. (B, C) Normalized peak tail current amplitude plotted against the duration of the intracellular perfusion (i.e., time after membrane rupture) without (B) or with cAMP/OA (C). The means of the WT or AT cells are shown by open and filled symbols, respectively. WT (N = 9), AT (N = 8) in panel B. WT (N = 8), AT (N = 8) in panel C. NS, $p \geq 0.05$, MANOVA.

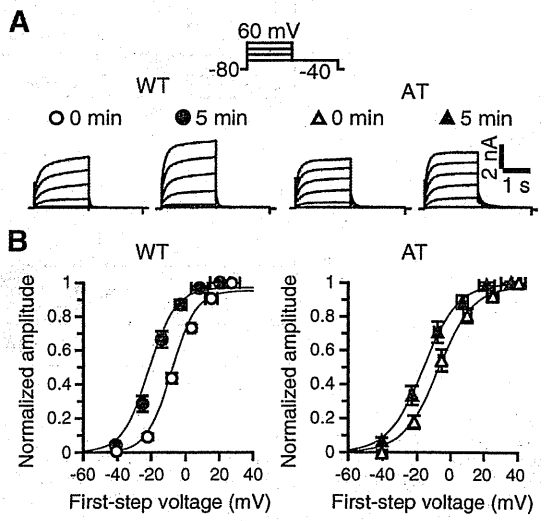

Fig. 6. cAMP/OA effects on the I_{Ks} voltage-dependency of KCNQ1(WT) and KCNQ1(A590T). (A) I_{Ks} was examined by comparing the currents recorded immediately after (0 min) and 5 min after membrane rupture. The cells were transfected with EGFP, KCNE1, Yotiao and either KCNQ1(WT) or KCNQ1(A590T) (WT and AT cells, respectively). The current was activated by 4 s depolarizing pulses (V_{first}, −40 to 60 mV; increment, 20 mV) followed by a 4 s repolarizing pulse (−40 mV). Representative current traces from WT or AT cells immediately after membrane rupture and 5 min after the rupture when the cAMP/OA intracellular perfusion sufficiently works. Representative current traces acquired at 0 min or 5 min were shown. (B) Plots indicate mean normalized peak current density–V_{first} relations. The data obtained at 0 min and 5 min are shown by open (0 min) and filled (5 min) symbols, respectively. WT (N = 7), AT (N = 6). Only in this experiment, errors in V_{first} due to the series resistance were corrected post hoc (see Supplemental methods). Smooth curves indicate the Boltzmann functions fitted to the collection of all the adopted data.

KCNQ1(WT) subunit alone (Fig. 2). This result suggests that KCNQ1(A590T) subunit does not have a dominant-negative effect on KCNQ1(WT) subunit, consistent with the previously reported mutations [23,29–31]. Several mutations in helix D including A590T have been suggested not to impede KCNQ1 subunit assembly [11,34]. Thus, the rescue of I_{Ks} amplitude and KCNQ1(A590T) subunit surface expression by co-expressed KCNQ1(WT) subunit in the WT/AT cells might be due to the heteromeric assembly of KCNQ1(WT) and KCNQ1(A590T) subunits (Figs. 2, 3).

As compared with the A590T mutation, the A590W mutation is reported to show a high extent of reduction of I_{Ks} (76%) [11]. Such a severe effect could be ascribed to possibly drastic changes in the size and property of alanine-to-tryptophan replacement. Despite the difference of the extents of the effects, the A590W and A590T mutations commonly resulted in diminished I_{Ks} channel expression without much affecting subunit assembly. These results raise a possibility that A590 might play a role in the mediation of interaction between KCNQ1 and other molecules rather than the assembly of KCNQ1 subunits.

It is known that I_{Ks} plays a primary role for controlling the repolarization of cardiac action potentials in response to sympathetic nervous stimulation. For example, when the sympathetic nerve is active, signaling through the β-adrenergic receptor-cAMP cascade results in I_{Ks} augmentation, which in turn accelerates the termination of cardiac action potentials and increases the heartbeat. The β-adrenergic receptor-mediated increase of intracellular cAMP leads to the activation of the serine/threonine kinase, protein kinase A (PKA). PKA is recruited to the I_{Ks} channel via the anchoring protein Yotiao, and phosphorylates S27 of KCNQ1 [13]. This phosphorylation is shown to be required for sympathetic regulation of I_{Ks} [13]. Previous studies have suggested that the KCNQ1(G589D) mutation disrupts the interaction of KCNQ1 with Yotiao, leading to a loss of β-adrenergic receptor-mediated modulation of the channel [13,27,28]. Our immunoprecipitation experiments showed that the A590T mutation did not affect the complex formation of KCNQ1 subunit with Yotiao and KCNE1subunit (Fig. 4). Moreover, our electrophysiological analysis showed that cAMP/OA-responsiveness was not different between homomeric KCNQ1(WT) channel and homomeric KCNQ1(A590T) channel (Figs. 5, 6). These results indicate that A590 is not a critical component of the KCNQ1/KCNE1/Yotiao interaction.

The previous studies have reported that the G589D mutation disrupts the interaction of the KCNQ1 subunit with Yotiao [13], and this results in massive reduction of membrane trafficking and I_{Ks} density [25, 26]. We confirmed that the cells transfected with KCNQ1(G589D), KCNE1, and Yotiao produced only small tail currents, consistent with the previous reports. However, we observed that intracellularly applied cAMP/OA augmented I_{Ks} in these cells (Supplemental Fig. 4). Together with the normal subunit assembly and interaction between KCNE1 and Yotiao (Fig. 4), the loss of functional I_{Ks} in the presence of the A590T or G589D mutation could be attributable to an impairment in membrane trafficking rather than disruption of Yotiao-mediated complex formation and cAMP-dependent channel modulation. To elucidate this hypothesis, further studies to seek for alternative mechanisms involved in I_{Ks} channel trafficking are required.

In summary, functional characterization of the KCNQ1(A590T) subunit showed that this mutation decreased the membrane trafficking and I_{Ks} density without affecting cAMP-dependent modulation of I_{Ks}, or interaction with Yotiao. In addition, co-expression of the KCNQ1(A590T) subunit with the KCNQ1(WT) subunit rescued these deficits, suggesting that heterozygous inheritance of KCNQ1(A590T) may not lead to severe cardiac disorders. Moreover, this might underlie the fact that the KCNQ1(A590T) carrier symptoms described in this and the previous reports are relatively mild [19,35,36]. Our data indicate that the A590 residue of the KCNQ1 subunit plays an important role in the cell surface expression of the I_{Ks} channel via a mechanism independent of channel assembly or interaction with Yotiao. These findings promote the understanding of the genotype–phenotype relations of inherited arrhythmic disorders.

Funding

This work was supported by a grant from the First Bank of Toyama Foundation (Toyama, Japan) and partly by a KAKENHI grant (#24790745) from the Ministry of Education, Culture, Sports, Science and Technology, Japan.

Disclosures

None declared.

Acknowledgments

We thank the provider of the gene sample for her kind cooperation.

Appendix A. Supplementary data

Supplementary data to this article can be found online at http://dx.doi.org/10.1016/j.yjmcc.2014.03.019.

References

[1] Wang Q, Curran ME, Splawski I, Burn TC, Millholland JM, VanRaay TJ, et al. Positional cloning of a novel potassium channel gene: *KVLQT1* mutations cause cardiac arrhythmias. Nat Genet 1996;12:17–23.
[2] Yang WP, Levesque PC, Little WA, Conder ML, Shalaby FY, Blanar MA. KvLQT1, a voltage-gated potassium channel responsible for human cardiac arrhythmias. Proc Natl Acad Sci U S A 1997;94:4017–21.
[3] Jespersen T, Grunnet M, Olesen SP. The KCNQ1 potassium channel: from gene to physiological function. Physiology 2005;20:408–16.
[4] Ravens U, Cerbai E. Role of potassium currents in cardiac arrhythmias. Europace 2008;10:1133–7.
[5] Chiang CE, Roden DM. The long QT syndromes: genetic basis and clinical implications. J Am Coll Cardiol 2000;36:1–12.
[6] Keating MT, Sanguinetti MC. Molecular and cellular mechanisms of cardiac arrhythmias. Cell 2001;104:569–80.
[7] Wilde AA, Roden DM. Predicting the long-QT genotype from clinical data: from sense to science. Circulation 2000;102:2796–8.
[8] Haitin Y, Attali B. The C-terminus of Kv7 channels: a multifunctional module. J Physiol 2008;586:1803–10.
[9] Ghosh S, Nunziato DA, Pitt GS. KCNQ1 assembly and function is blocked by long-QT syndrome mutations that disrupt interaction with calmodulin. Circ Res 2006;98:1048–54.
[10] Shamgar L, Ma L, Schmitt N, Haitin Y, Peretz A, Wiener R, et al. Calmodulin is essential for cardiac I_{Ks} channel gating and assembly: impaired function in long-QT mutations. Circ Res 2006;98:1055–63.
[11] Wiener R, Haitin Y, Shamgar L, Fernandez-Alonso MC, Martos A, Chomsky-Hecht O, et al. The KCNQ1 (Kv7.1) COOH terminus, a multitiered scaffold for subunit assembly and protein interaction. J Biol Chem 2008;283:5815–30.
[12] Nakajo K, Kubo Y. Second coiled-coil domain of KCNQ channel controls current expression and subfamily specific heteromultimerization by salt bridge networks. J Physiol 2008;586:2827–40.
[13] Marx SO, Kurokawa J, Reiken S, Motoike H, D'Armiento J, Marks AR, et al. Requirement of a macromolecular signaling complex for β adrenergic receptor modulation of the KCNQ1-KCNE1 potassium channel. Science 2002;295:496–9.
[14] Kurokawa J, Motoike HK, Rao J, Kass RS. Regulatory actions of the A-kinase anchoring protein Yotiao on a heart potassium channel downstream of PKA phosphorylation. Proc Natl Acad Sci U S A 2004;101:16374–8.
[15] Chen L, Marquardt ML, Tester DJ, Sampson KJ, Ackerman MJ, Kass RS. Mutation of an A-kinase-anchoring protein causes long-QT syndrome. Proc Natl Acad Sci U S A 2007;104:20990–5.
[16] Dessauer CW. Adenylyl cyclase–A-kinase anchoring protein complexes: the next dimension in cAMP signaling. Mol Pharmacol 2009;76:935–41.
[17] Li Y, Chen L, Kass RS, Dessauer CW. The A-kinase anchoring protein Yotiao facilitates complex formation between adenylyl cyclase type 9 and the I_{Ks} potassium channel in heart. J Biol Chem 2012;287:29815–24.
[18] Splawski I, Shen J, Timothy KW, Lehmann MH, Priori S, Robinson JL, et al. Spectrum of mutations in long-QT syndrome genes. *KVLQT1*, *HERG*, *SCN5A*, *KCNE1*, and *KCNE2*. Circulation 2000;102:1178–85.
[19] Tester DJ, Will ML, Haglund CM, Ackerman MJ. Compendium of cardiac channel mutations in 541 consecutive unrelated patients referred for long QT syndrome genetic testing. Heart Rhythm 2005;2:507–17.
[20] Yang P, Kanki H, Drolet B, Yang T, Wei J, Viswanathan PC, et al. Allelic variants in long-QT disease genes in patients with drug-associated torsades de pointes. Circulation 2002;105:1943–8.
[21] Neyroud N, Richard P, Vignier N, Donger C, Denjoy I, Demay L, et al. Genomic organization of the *KCNQ1* K^+ channel gene and identification of C-terminal mutations in the long-QT syndrome. Circ Res 1999;84:290–7.

[22] Itoh T, Tanaka T, Nagai R, Kikuchi K, Ogawa S, Okada S, et al. Genomic organization and mutational analysis of *KVLQT1*, a gene responsible for familial long QT syndrome. Hum Genet 1998;103:290–4.
[23] Yamashita F, Horie M, Kubota T, Yoshida H, Yumoto Y, Kobori A, et al. Characterization and subcellular localization of KCNQ1 with a heterozygous mutation in the C terminus. J Mol Cell Cardiol 2001;33:197–207.
[24] Biliczki P, Girmatsion Z, Brandes RP, Harenkamp S, Pitard B, Charpentier F, et al. Trafficking-deficient long QT syndrome mutation KCNQ1-T587M confers severe clinical phenotype by impairment of KCNH2 membrane localization: evidence for clinically significant IKr–IKs alpha-subunit interaction. Heart Rhythm 2009;6:1792–801.
[25] Kanki H, Kupershmidt S, Yang T, Wells S, Roden DM. A structural requirement for processing the cardiac K^+ channel KCNQ1. J Biol Chem 2004;279:33976–83.
[26] Piippo K, Swan H, Pasternack M, Chapman H, Paavonen K, Viitasalo M, et al. A founder mutation of the potassium channel KCNQ1 in long QT syndrome: implications for estimation of disease prevalence and molecular diagnostics. J Am Coll Cardiol 2001;37:562–8.
[27] Saucerman JJ, Healy SN, Belik ME, Puglisi JL, McCulloch AD. Proarrhythmic consequences of a KCNQ1 AKAP-binding domain mutation: computational models of whole cells and heterogeneous tissue. Circ Res 2004;95:1216–24.
[28] Heijman J, Spatjens RL, Seyen SR, Lentink V, Kuijpers HJ, Boulet IR, et al. Dominant-negative control of cAMP-dependent I_{Ks} upregulation in human long-QT syndrome type 1. Circ Res 2012;110:211–9.
[29] Grunnet M, Behr ER, Calloe K, Hofman-Bang J, Till J, Christiansen M, et al. Functional assessment of compound mutations in the *KCNQ1* and *KCNH2* genes associated with long QT syndrome. Heart Rhythm 2005;2:1238–49.
[30] Huang L, Bitner-Glindzicz M, Tranebjaerg L, Tinker A. A spectrum of functional effects for disease causing mutations in the Jervell and Lange-Nielsen syndrome. Cardiovasc Res 2001;51:670–80.
[31] Westenskow P, Splawski I, Timothy KW, Keating MT, Sanguinetti MC. Compound mutations: a common cause of severe long-QT syndrome. Circulation 2004;109:1834–41.
[32] Wilson AJ, Quinn KV, Graves FM, Bitner-Glindzicz M, Tinker A. Abnormal KCNQ1 trafficking influences disease pathogenesis in hereditary long QT syndromes (LQT1). Cardiovasc Res 2005;67:476–86.
[33] Sato A, Arimura T, Makita N, Ishikawa T, Aizawa Y, Ushinohama H, et al. Novel mechanisms of trafficking defect caused by *KCNQ1* mutations found in long QT syndrome. J Biol Chem 2009;284:35122–33.
[34] Howard RJ, Clark KA, Holton JM, Minor Jr DL. Structural insight into KCNQ (Kv7) channel assembly and channelopathy. Neuron 2007;53:663–75.
[35] Lupoglazoff JM, Denjoy I, Villain E, Fressart V, Simon F, Bozio A, et al. Long QT syndrome in neonates: conduction disorders associated with *HERG* mutations and sinus bradycardia with *KCNQ1* mutations. J Am Coll Cardiol 2004;43:826–30.
[36] Novotny T, Kadlecova J, Papousek I, Chroust K, Bittnerova A, Florianova A, et al. Mutational analysis of LQT genes in individuals with drug induced QT interval prolongation. Vnitr Lek 2006;52:116–8.
[37] Ehrlich JR, Zicha S, Coutu P, Hebert TE, Nattel S. Atrial fibrillation-associated minK38G/S polymorphism modulates delayed rectifier current and membrane localization. Cardiovasc Res 2005;67:520–8.
[38] Girmatsion Z, Biliczki P, Takac I, Schwerthelm C, Hohnloser SH, Ehrlich JR. N-terminal arginines modulate plasma-membrane localization of $K_V7.1$/KCNE1 channel complexes. PLoS One 2011;6:e26967.
[39] Schwake M, Athanasiadu D, Beimgraben C, Blanz J, Beck C, Jentsch TJ, et al. Structural determinants of M-type KCNQ (K_V7) K^+ channel assembly. J Neurosci 2006;26:3757–66.
[40] Xu Q, Minor Jr DL. Crystal structure of a trimeric form of the $K_V7.1$ (KCNQ1) A-domain tail coiled-coil reveals structural plasticity and context dependent changes in a putative coiled-coil trimerization motif. Protein Sci 2009;18:2100–14.

Int J Legal Med (2014) 128:105–115
DOI 10.1007/s00414-013-0853-4

ORIGINAL ARTICLE

Identification and characterization of a novel genetic mutation with prolonged QT syndrome in an unexplained postoperative death

Yukiko Hata · Hisashi Mori · Ayumi Tanaka · Yosuke Fujita · Takeshi Shimomura · Toshihide Tabata · Koshi Kinoshita · Yoshiaki Yamaguchi · Fukiko Ichida · Yoshihiko Kominato · Noriaki Ikeda · Naoki Nishida

Received: 29 January 2013 / Accepted: 19 March 2013 / Published online: 2 April 2013

Abstract
Introduction The human *ether-à-go-go*-related gene (*hERG*) encodes the α-subunit of a cardiac potassium channel. Various mutations of *hERG*, including missense mutations, have been reported to cause long QT syndrome (LQTS) and severe arrhythmic disorders such as sudden cardiac death. We identified a novel *hERG* frameshift mutation (*hERG*(ΔAT)) in the S5-pore region from a LQTS patient who died suddenly and analyzed its genetic profile and the molecular and electrophysiological behaviors of the protein product to assess the pathogenicity of *hERG*(ΔAT).
Methods and results We performed direct sequencing of *hERG* and evaluated its transcript level by using a whole blood sample from the patient. We performed immunoblotting, immunocytochemistry, and patch-clamp recordings of HEK-293 T cells transfected with *hERG*(ΔAT), wild-type *hERG* (*hERG*(WT)), or both. The patient demonstrated an AT deletion (c.1735_1736del) in *hERG* and a decrease in

The nucleotide sequence reported in this paper has been submitted to GenBank under accession number JX261933.

Y. Hata · K. Kinoshita · N. Nishida (✉)
Department of Legal Medicine, Faculty of Medicine, Graduate School of Medicine and Pharmaceutical Sciences for Research, University of Toyama, 2630 Sugitani,
Toyama 930-0194, Japan
e-mail: nishida@med.u-toyama.ac.jp

H. Mori · A. Tanaka
Department of Molecular Neuroscience, Graduate School of Medicine and Pharmaceutical Sciences for Research, University of Toyama, 2630 Sugitani,
Toyama 930-0194, Japan

Y. Fujita · T. Shimomura · T. Tabata
Laboratory for Neural Information Technology, Graduate School of Sciences and Engineering, University of Toyama, 3190 Gofuku,
Toyama 930-8555, Japan

Y. Yamaguchi
Second Department of Internal Medicine, Graduate School of Medicine and Pharmaceutical Sciences for Research, University of Toyama, 2630 Sugitani,
Toyama 930-0194, Japan

F. Ichida
Department of Pediatrics, Graduate School of Medicine and Pharmaceutical Sciences for Research, University of Toyama, 2630 Sugitani,
Toyama 930-0194, Japan

Y. Kominato
Department of Legal Medicine, Graduate School of Medicine, Gunma University, 3-39-22 Showa-machi,
Maebashi 371-8511, Japan

N. Ikeda
Department of Forensic Pathology and Sciences, Graduate School of Medical Sciences, Kyushu University,
3-1-1 Maidashi, Higashi-ku,
Fukuoka 812-8582, Japan

*h*ERG mRNA transcripts. HEK-293 T cells showed lower production and cell surface expression of hERG(ΔAT) compared with hERG(WT) protein. In addition, the hERG(ΔAT) protein failed to form functional channels, while the activation kinetics of functional channels, presumably consisting of hERG(WT) subunits, were unaffected.

Conclusion The ΔAT mutation may decrease the number of functional hERG channels by impairing the posttranscriptional and posttranslational processing of the mutant product. This decrease may partly explain the cardiac symptoms of the patient who was heterozygous for *hERG*(ΔAT).

Keywords M579fs+75X frameshift mutation · Human *ether-à-go-go*-related gene · Long QT syndrome · Patch-clamp · Transmembrane pore domain · Arrhythmia

Introduction

Long QT syndrome (LQTS) is a congenital disorder that predisposes patients to sudden cardiac death (SCD) [1, 2]. The phenotypic and genetic heterogeneity of LQTS are widely accepted. The clinical history and electrocardiographic phenotype of LQTS can range from complete absence of symptoms and a normal resting electrocardiograph (ECG) to sudden death in infancy resulting from extreme QT prolongation [3]. Such phenotypic variability can make clinical diagnosis challenging. To date, LQTS has been attributed to mutations in 13 genes [4, 5]. Approximately 90 % of genotyped LQTS patients belong to type 1 LQT (LQT1), LQT2, or LQT3. LQTS has been shown to be an ion channelopathy associated with loss-of-function mutations in genes encoding repolarizing potassium channels, their subunits, and certain interacting proteins. Gain-of-function mutations in genes encoding depolarizing sodium and calcium channels have also been associated with LQTS [6]. LQTS-associated genes are listed in Table 1.

Nearly 300 LQT2-linked missense, frameshift, deletion, insertion, and nonsense mutations of the human *ether-à-go-go*-related gene (*hERG*) have been identified. *hERG* mutations can cause channel malfunction via diverse mechanisms, including abnormal channel protein processing, generation of nonfunctional protein, dominant-negative suppression, and alterations in channel gating [7]. More than 30 % of the *hERG* mutations identified are nonsense/frameshift mutations that introduce premature termination codons. These nonsense/frameshift mutations are more frequently located in the C-terminal region of the hERG protein and less frequently in the transmembrane pore domain (S5–loop–S6) [8].

Here we report a novel *hERG* frameshift mutation in the S5-pore region (*hERG*(ΔAT)), identified during LQTS genetic screening of a patient who died from SCD. This patient displayed only mild corrected QT interval (QTc) prolongation during electrocardiography and had no prior symptoms. We also evaluated the *hERG* transcript level in the patient's blood. To elucidate the pathogenic mechanism of hERG(ΔAT), we examined the molecular and electrophysiological behaviors of the protein product by performing immunoblotting, immunocytochemistry, and patch-clamp recordings of hERG-transfected HEK-293 T cells.

Materials and methods

Subject characteristics

A 44-year-old woman died suddenly 10 h after awakening from general anesthesia for microscope-guided resection of a laryngeal granuloma. The histology of the extirpated specimen showed that it was nonspecific granuloma tissue. No neoplastic change, epithelioid granulomas, nor pathogens were found. Twelve-lead ECGs were obtained during the patient's preoperative examination. QT and RR intervals were measured on three consecutive sinus complexes in lead V_5. The QT value was corrected for heart rate according to Bazett's formula (QTc). The ECG demonstrated a prolonged QTc interval of 493 ms, but the patient had no clinical history of cardiac symptoms, such as syncope, near-syncope, or palpitations. No family history was available either. An autopsy was performed to clarify the cause of death. At autopsy, the heart weighed 320 g and was examined both macroscopically and microscopically using methods previously reported [9]. The heart showed mild dilatation of the left atrium and ventricle, mild thinning of the left ventricular walls, and hypertrabeculation of the papillary muscle of the left ventricle (Fig. 1a, b). The thickness of the anterior wall of the left ventricle, ventricular septum, and right ventricle was 1.3, 1.2, and 0.2 cm, respectively. The mitral leaflet was thickened and showed mild myxoid degeneration. The coronary arteries were normal in appearance. Histological specimens were taken from one or two circumferential horizontal sections at the levels of the papillary muscle and apex. The sinoatrial node and atrioventricular conduction systems were also examined. Histologically, the patient had above average degrees of interstitial fibrosis for her age in the left ventricle (Fig. 1c) and in the atrioventricular conduction system. No other clinically significant lesions were found, and these cardiac abnormalities were deemed insufficient to be the cause of death.

A control subject, a 36-year-old man, was heterozygous for a synonymous polymorphism (1692A/G) in *hERG* (*hERG*(L564L)) and lacked mutations in any other major arrhythmia-related genes. This control was used for analysis of mRNA isolated from whole blood.

Table 1 Genes associated with long QT syndrome

Gene	Type	Protein	Functional effect
KCNQ1	LQT1	I_{Ks} potassium channel α-subunit	Loss-of-function
hERG (*KCNH2*)	LQT2	I_{Kr} potassium channel α-subunit	Loss-of-function
SCN5A	LQT3	I_{Na} sodium channel α-subunit	Gain-of-function
ANK2	LQT4	Ankyrin B, anchoring protein	Loss-of-function
KCNE1	LQT5	I_{Ks} potassium channel β-subunit	Loss-of-function
KCNE2	LQT6	I_{Kr} potassium channel β-subunit	Loss-of-function
KCNJ2	LQT7	I_{K1} potassium channel α-subunit	Loss-of-function
CACNA1C	LQT8	I_{Ca} calcium channel α-subunit	Gain-of-function
CAV3	LQT9	Caveolin	Loss-of-function
SCN4B	LQT10	I_{Na} sodium channel β-subunit	Loss-of-function
AKAP9	LQT11	Yotiao, A-kinase-anchoring protein	Loss-of-function
SNTA1	LQT12	α1-Syntrophin	Loss-of-function
KCNJ5	LQT13	Kir3.4 subunit of I_{KAch} channel	Loss-of-function

Genetic analysis

Genomic DNA was extracted directly from whole blood using a QIAamp DNA Blood Mini Kit (Qiagen Science, MD, USA). Genomic DNA samples were PCR-amplified using primers designed to amplify the complete sequences of all five major arrhythmia-related genes [i.e., *KCNE1* (GenBank accession number, NM_00219.4), *KCNE2* (NM_172201.1), *KCNQ1* (NM_000218.2), *SCN5A* (NM_000335.4), and *hERG* (NM_000238.3)], cardiomyopathy-associated sarcomere genes [i.e., *MYH7* (NM_000257.2), *MYBPC3* (NM_000256.3), *TNNT2* (NM_000364.2), *ACTC1* (NM_005159.4), and *TPM1* (NM_001018005.1)], and desmosome genes [i.e., *PKP2* (NM_004572.3), *DSP* (NM_004415.2), *DSG2* (NM_001943.3), *JUP* (NM_002230.2), and *DGC2* (NM_024422.3)] [10]. The nucleotide sequences of the amplified fragments were analyzed by direct sequencing in both directions using the BigDye Terminator v3.1 Cycle Sequencing Kit (Applied Biosystems, CA, USA). Sequence analysis was performed using the ABI PRISM 3100-Avant Genetic Analyzer (Applied Biosystems). In addition, PCR products were subcloned into the pCR2.1 plasmid vector (Invitrogen, CA, USA).

Reverse transcription-PCR (RT-PCR)

Total RNA was isolated from whole blood that had been stored at −80 °C, and RT-PCR was performed as previously described [11]. *hERG* mRNA was reverse-transcribed and amplified using primers corresponding to sequences in exons 6 and 7 (Fig. 3). The sequences of the primers were as follows: Ex6F—5′ ACT ACT TCA AGG GCT GGT TCC TCA TCG 3′ and Ex7R—5′ AGT AGA GCG CCG

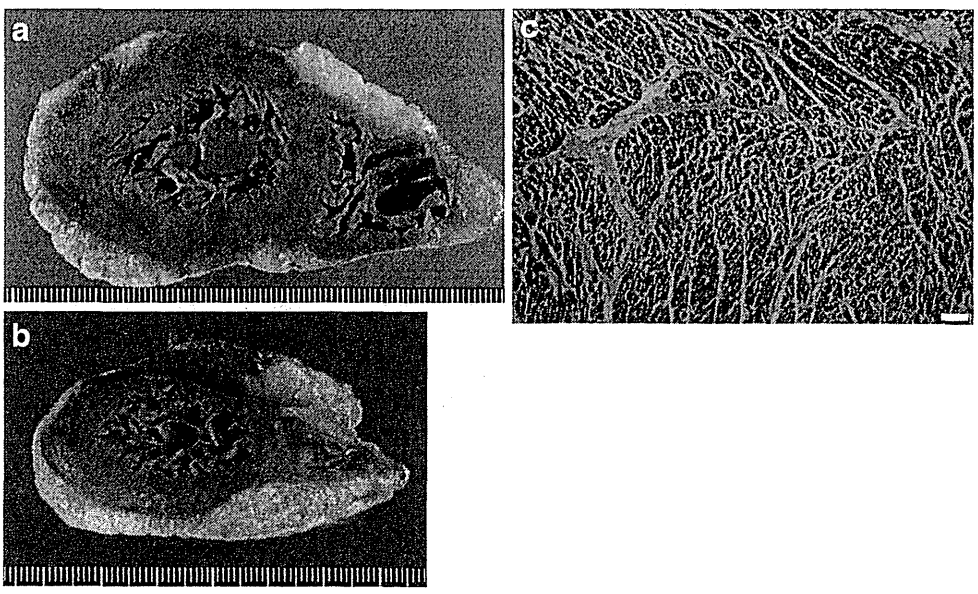

Fig. 1 Gross and microscopic appearance of the heart. **a**, **b** Horizontal sections of the ventricles. Hypertrabeculation of the left ventricle, especially the apex, was evident. **c** Left ventricle. Moderate fibrosis and endocardial thickening were present. Scale bar=100 μm

TCA CAT ACT TGT CC 3′. PCR cycling conditions were 94 °C for 1 min; 40 cycles of 94 °C for 1 min, 60 °C for 1 min, and 72 °C for 1 min; and 72 °C for 5 min. PCR amplifications were performed in 25 μL reaction mixtures containing 5 pmol of each primer, 1.3 U of *Ex Taq* DNA polymerase (Takara Bio Inc., Shiga, Japan), 200 μM dNTPs, and 1× GC buffer I (Takara). The amplified fragments were sequenced as described above.

Construction of *hERG*(WT) and *hERG*(ΔAT) expression vectors

The pSI-*hERG* expression vector [12] was kindly provided by Drs. Kenshi Hayashi (Kanazawa University Graduate School of Medical Science, Kanazawa, Japan) and Sabina Kupershmidt (Vanderbilt University, School of Medicine, Nashville, TN, USA). pSI-*hERG* was digested with *Bam*HI, followed by ligation with a linker DNA fragment containing *Bam*HI–*Sal*I–*Bam*HI sites to yield the plasmid pSI-*hERG*-BSB. The 1.4-kb fragment obtained after digesting pSI-*hERG* with *Xho*I and *Sal*I was subcloned into the *Xho*I site of the expression plasmid pCAGGS [13], which was a kind gift from Dr. Jun-ichi Miyazaki (Osaka University Medical School, Osaka, Japan), to construct the plasmid pCAG-*hERG*-XS. The 2.1-kb fragment obtained after digesting pSI-*hERG* with *Xho*I was subcloned into the *Xho*I site of pBluescript II (Clontech Laboratory Inc., CA, USA) to generate pBS-H-Xh2.1. The 266-bp DNA fragment containing the ΔAT mutation was constructed through two-step PCR [14] using the appropriate primers and pBS-H-Xh2.1 as a template, followed by digestion with *Nhe*I and ligation with *Nhe*I-digested wild-type pBS-H-Xh2.1 to yield plasmid pBS-H-Xh2.1-ΔAT. The 2.1-kb fragments of *hERG*(WT) and *hERG*(ΔAT), obtained from *Xho*I digestion of pSI-*hERG* and pBS-H-Xh2.1-ΔAT, respectively, were subcloned individually into the *Xho*I site of pCAG-*hERG*-XS to construct the expression vectors pCAG-*hERG*(WT) and pCAG-*hERG*(ΔAT), respectively.

DNA fragments encoding double hemagglutinin (HA) tags (GGG GSY PYD VPD YAG GGG SYP YDV PDY A) or double myelocytomatosis viral oncogene (Myc) tags (GGG GSA SMQ KLI SEE DLG GGG SAS MQK LIS EED L) flanked by linkers were prepared by annealing the appropriate oligonucleotide DNAs. The HA-tag was attached to the C-terminus of *hERG*(WT) and the Myc-tag to the C-terminus of *hERG*(ΔAT) through the inverse PCR method [15], using a KOD-plus mutagenesis kit (Toyobo, Tokyo, Japan). The 1.1-kb *Sac*I–*Hin*dIII fragment containing the HA-tag was replaced with the *Sac*I-*Hin*dIII-digested fragment of *hERG*(WT) to yield HA-tagged *hERG*(WT). The 1.2-kb *Bst*EII–*Sph*I fragment containing the Myc-tag was replaced with the *Bst*EII–*Sph*I fragment of *hERG*(ΔAT) to yield Myc-tagged *hERG*(ΔAT).

Cell culture and DNA transfection

Human embryonic kidney (HEK) 293 T cells (no. CRL-11268, American Type Culture Collection, VA, USA) were grown in Dulbecco's modified Eagle's medium supplemented with 10 % fetal bovine serum and 0.5 % penicillin–streptomycin at 37 °C and 5 % CO_2. Briefly, 2.0×10^5 HEK-293 T cells were seeded into a 35-mm dish the day before transfection. Construct plasmid DNA was added onto the cell monolayer (0.5 μg for Western blot analysis; 225 ng for patch-clamp recordings; or 1 μg for immunocytochemistry), as well as 10 μL TransIT-293 transfection reagent (Mirus, WI, USA) in 1 mL Dulbecco's modified Eagle's medium, according to the manufacturer's instructions. The p*EGFP*-N1 vector (Clontech) encoding enhanced green fluorescent protein (GFP) was co-transfected with the plasmid construct, and the target cells were identified by fluorescence microscopy. At 48 h post-transfection, the cells were scraped from the plates for Western blotting, fixed according to standard protocols for immunocytochemistry, or trypsinized as standards for patch-clamp recordings.

Western blotting

After the 48-h incubation, HEK-293 T cells transiently transfected with *hERG*(WT) and *hERG*(ΔAT) were washed with phosphate-buffered saline (PBS; pH 7.4), homogenized in mammalian protein extraction reagent (M-PER, Thermo Scientific, IL, USA), and centrifuged at 17,800×*g* for 10 min. Protein concentrations in the supernatants were determined using the BCA Protein Assay Kit (Thermo Scientific). The extracted protein samples were heat-denatured, electrophoresed in 7.5 % sodium dodecyl sulfate-polyacrylamide gels, and transferred to a polyvinylidene difluoride membrane (GE Healthcare, Tokyo, Japan). The membrane was blocked with 5 % skim milk in Tris-based buffer (TBS; 20 mM Tris–HCl, pH 7.6, 137 mM NaCl) containing 0.1 % Tween-20 (TBST) for 1 h. The polyclonal anti-hERG antibody (Santa Cruz Biotechnology, CA, USA) used in the present study was raised in rabbits against amino acids 96–270, which lie near the N-terminus of human hERG. The membrane was incubated with rabbit anti-hERG antibody (1:200 dilution) overnight at 4 °C, washed the next day in TBST, and incubated with a secondary antibody (1:10,000 dilution; goat anti-rabbit IgG HRP, Bio-Rad, Tokyo, Japan) at room temperature for 1 h. The membrane was washed again in TBST, and protein bands were detected using the ECL Prime Western Blotting Detection System (GE Healthcare) with a lumino-imaging analyzer (ImageQuant LAS-4000, Fujifilm, Tokyo, Japan).

Immunocytochemistry and confocal microscopy

HEK-293 T cells (2.5×10^5 cells per dish) were seeded on polyethyleneimine-coated 35 mm glass-based dishes (Iwaki, Chiba, Japan). After 24 h of incubation, the cells were co-transfected with the plasmids HA-tagged *hERG*(WT) and Myc-tagged *hERG*(ΔAT). The cells were cultured for 48 h, fixed in 4 % paraformaldehyde for 10 min at room temperature, permeabilized with 0.1 % Triton X-100 in PBS for 5 min, and then incubated in blocking solution (PBS containing 5 % goat serum) for 30 min. Subsequently, the cells were incubated overnight in PBS containing rat monoclonal anti-HA antibody (1:800 dilution; Roche Diagnostics, IN, USA) and rabbit polyclonal anti-Myc antibody (1:125 dilution, Santa Cruz Biotechnology) at 4 °C. The next day, the cells were washed in PBS and incubated with goat anti-rat IgG Alexa Fluor 568 (1:500 dilution; Invitrogen) and goat anti-rabbit IgG Alexa Fluor 647 (1:500 dilution; Invitrogen) at room temperature for 1 h. The cells were washed in PBS, and the nuclei were stained using 4′,6-diamidino-2-phenylindole. Images were obtained by confocal laser microscopy (TCS SP5, Leica, IL, USA).

Electrophysiology

Ruptured-patch whole cell voltage-clamp recordings were performed. A recording pipette was pulled from a glass capillary to a tip resistance of ~5 MΩ and filled with a solution comprising 134 mM potassium D-gluconic acid, 7.6 mM KCl, 9 mM KOH, 10 mM NaCl, 1.2 mM $MgCl_2$, 10 mM HEPES, 0.5 mM EGTA, and 4 mM ATP magnesium salt (pH adjusted to 7.3 with D-gluconic acid). The recording bath was perfused at a rate of 0.7 mL/min with 147 mM NaCl, 3 mM KCl, 2 mM $CaCl_2$, 1 mM $MgCl_2$, 10 mM HEPES, and 10 mM D-glucose (pH adjusted to 7.4 with NaOH). The command voltages were corrected for the liquid junction potential between the pipette and bath solutions. Current signals were acquired using an EPC 9 Double amplifier (HEKA, Lambrecht, Germany; cut-off frequency 2 or 5 kHz; sampling frequency 5 or 50 kHz) that was controlled using Pulse software (version 8.53; HEKA). The holding voltage was −80 mV.

After a recording configuration was established, the pipette capacitance was canceled electronically, and current responses to 10 bipolar voltage pulses (amplitude ±5 mV; duration 40 ms) were recorded. The cell membrane capacitance (C_m) was then canceled electronically, and whole cell currents were recorded at an electronic series resistance compensation of 60 %. After the recordings, the passive cell membrane conductance and C_m were estimated from the average of the pulse-evoked current responses and used for off-line linear leakage subtraction and calculation of the current density (i.e., current amplitude per unit C_m). Function fitting to the data were performed using JMP software (version 7.0.2, SAS Institute, NC, USA). To evaluate the voltage dependence of activation, a Boltzmann equation ($I_{hERG}=A/[1+(V_{half}-V_{comm})/K]$, where I_{hERG}, A, V_{half}, V_{comm}, and K are the amplitude of hERG channel current, scale factor, voltage for half-maximal activation, command potential, and slope, respectively) was fitted to the current density-command potential plot for each cell. The time constant was estimated from the single-exponential curve fitted to the rising phase (a range of first-step duration from zero to the point at which the activation extent became saturated) of the plot of activation extent against first-step duration (cf. Fig. 6d) for each cell.

Data from numerical data groups are presented as mean± SEM. Significant differences (i.e., $P<0.05$) between numerical data groups were evaluated using the van der Waerden rank-sum test because the majority of the groups were judged to have non-normal distribution according to the Shapiro–Wilk test.

Results

Genetic studies

Among major arrhythmia-related genes including *KCNE1*, *KCNE2*, *KCNQ1*, *SCN5A*, and *hERG*, only *hERG* demonstrated any mutation—in this case, a heterozygous AT deletion (c.1735_1736del), which gave rise to the mutant gene *hERG*(ΔAT) (Fig. 2a). This deletion changes the amino acid at position 579 and causes a shift in the reading frame resulting in the generation of a premature stop codon at amino acid 653 (p.M579fs+75X). The deletion therefore creates a new amino acid sequence between position 579 and 74 residues downstream, instead of the C-terminal 581 amino acids that occur in the WT protein (Fig. 2b). This allele therefore encodes a truncated protein that lacks the pore-S6 region and the C-terminus (Fig. 2c). Because amino acids 579–1159 (which comprise the S5-pore region and C-terminus of hERG) include domains required for appropriate tetramerization, maturation, stability, and surface expression of hERG channels [7], this AT deletion may lead to a loss-of-function mutant protein. Within the desmosome genes (*PKP2*, *DSP*, *DSG2*, *JUP*, and *DSC2*) sequenced, two previously published nonsynonymous polymorphisms [16] were also identified, one in *DSP* (p.R1738A) and the other in *JUP* (p.M697L). No mutations were found in *PKP2*, *DSG2*, or *DSC2*. We did not identify any mutations in the sarcomere genes (*MYH7*, *MYBPC3*, *TNNT2*, *ACTC1*, or *TPM1*).

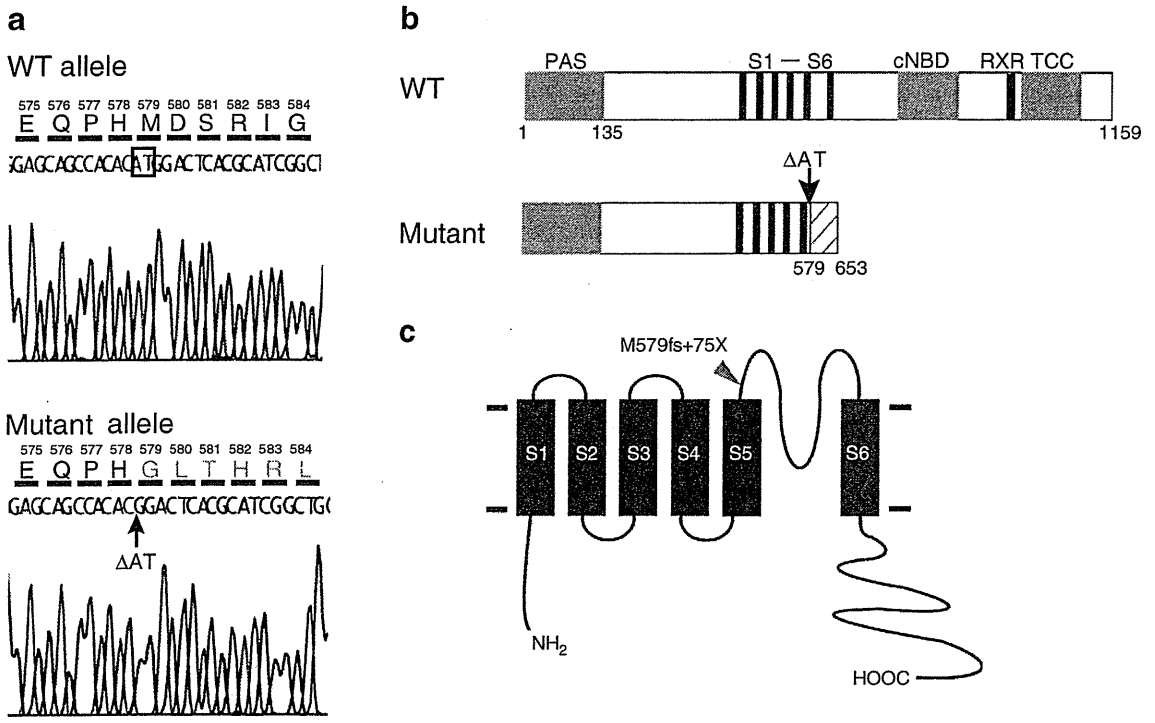

Fig. 2 Sequence analysis of exon 7 in *hERG*. **a** Direct sequencing revealed a 2-bp deletion of nucleotides 1735–1736 in exon 7 of *hERG*. The putative amino acid sequence is shown above the nucleotide sequence. **b** Schematic diagram of the *hERG* subunit, showing the location of the hERG truncation mutation and domains or regions proposed to be involved in hERG channel assembly and trafficking. PAS: Per, Arnt, and Sim domains; S1–S6: transmembrane domain; S1–S4: voltage sensor domain; S5–S6: K^+ selective pore; cNBD: cyclic nucleotide binding domain (residues 750–870); RXR: ER retention motif (residues 1005–1007); TCC: tetramerizing coiled-coil domain (residues 1018–1122). **c** Schematic representation of the predicted topology of the wild-type *hERG* potassium channel and the location of the deletion (*orange triangle*)

Analysis of mRNA isolated from whole blood

To determine the pathogenic effects of *hERG*(ΔAT), we used RT-PCR to analyze the *hERG* transcripts in the subject. We prepared RNA from whole blood samples from both the patient and the control subject. cDNA synthesized from DNase I-treated RNA was used as a template for PCR amplification (Fig. 3a). The RT-PCR products of *hERG* transcripts in the *hERG*(ΔAT) subject and the control both showed an approximately 370-bp band by electrophoresis (Fig. 3b). Direct sequencing of the RT-PCR products of the patient revealed the presence of transcripts from both wild-type (*hERG*(WT)) and mutant (*hERG*(ΔAT)) alleles. However, in the chromatograms, the sequence corresponding to the *hERG*(ΔAT) allele had lower peaks (Fig. 3c), suggesting that fewer transcripts were derived from the *hERG*(ΔAT) allele than from the *hERG*(WT) allele. To rule out the possibility of allelic variation in *hERG* mRNA expression, we compared the levels of transcripts derived from the 1692A and 1692G alleles of the control. The results indicated almost equal levels of transcripts from these two alleles, suggesting a lack of allelic variation in *hERG* mRNA expression of common alleles.

Expression of hERG(WT) and hERG(ΔAT) channel subunits in HEK-293 T cells

We used Western blot analysis to assess the expression of wild-type or mutant channel subunits in HEK-293 T cells that were transfected with *hERG*(WT) and *hERG*(ΔAT) cDNA. The anti-hERG antibody recognized bands corresponding to proteins larger than ~135 kDa in *hERG*(WT)-transfected cells and a protein of ~76 kDa in *hERG*(ΔAT)-transfected cells (Fig. 4). The sizes of the main proteins detected for the hERG(WT) and hERG(ΔAT) subunits are consistent with that reported for the wild-type subunit [17] and the expected size of the truncated protein. The amount of hERG(WT) protein detected was at least 50 times that of the hERG(ΔAT) protein (Fig. 4). In addition, the ratio of the protein expression levels of the hERG(WT) and hERG(ΔAT) subunits in HEK-293 T cells that were co-transfected with *hERG*(WT) and *hERG*(ΔAT) cDNAs was similar to the ratio of the protein levels in singly transfected cells. These results suggest that the hERG(ΔAT) subunit protein was expressed at a lower level than that of the hERG(WT) subunit and that the expression of wild-type and mutant channel subunits did not interfere with each other.

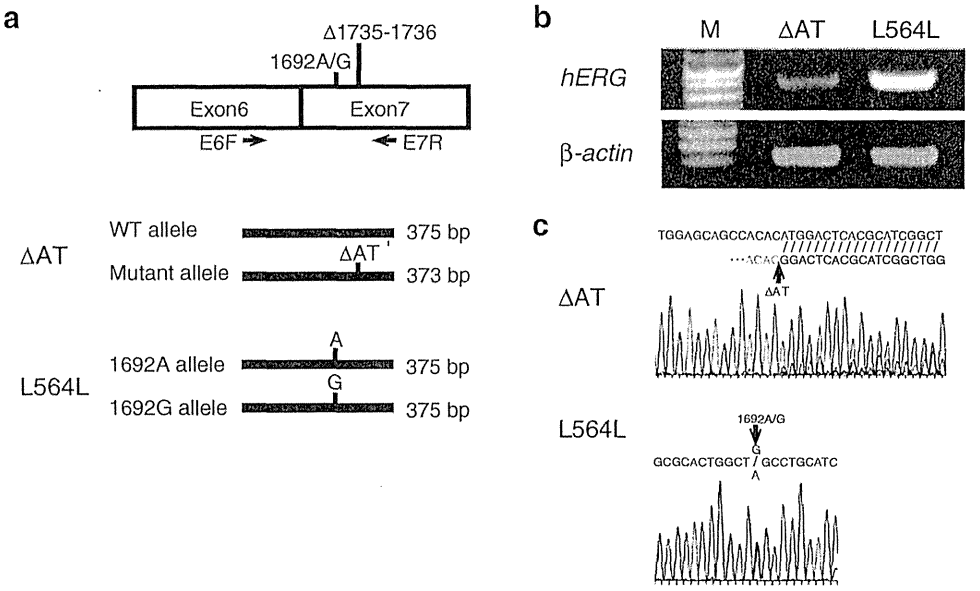

Fig. 3 Expression of *hERG* in blood cells. **a** Schematic diagram showing the position of the mutation and the sizes of the nucleotide fragments from alleles of the *hERG*(ΔAT) carrier, (ΔAT), and the 1692A/G carrier, (L564L). Forward primer E6F in exon 6 and reverse primer E7R in exon 7 were used in the RT-PCR analysis. **b** Using RT-PCR analysis, the expression levels of *hERG* and *β-actin* were determined in whole blood samples from both the *hERG*(ΔAT) and the 1692A/G carrier. **c** Direct sequencing of the gel-extracted RT-PCR products demonstrated that they were derived from both *hERG*(WT) (major) and *hERG*(ΔAT) (minor) transcripts. In contrast, the PCR products derived from the 1692A/G alleles (hERG(L564L)) arose from equal amounts of transcripts from both alleles

Subcellular localization and expression of hERG(WT) and hERG(ΔAT) channel subunits

To reveal the heterologous expression of hERG(WT) and hERG(ΔAT) channel subunits in HEK-293 T cells, we constructed C-terminally HA-tagged *hERG*(WT) and Myc-tagged *hERG*(ΔAT) expression vectors. We then co-transfected these tagged expression vectors into HEK-293 T cells and used confocal microscopy and anti-HA and anti-Myc antibodies to examine the subcellular localization and expression of these subunits. We detected cells

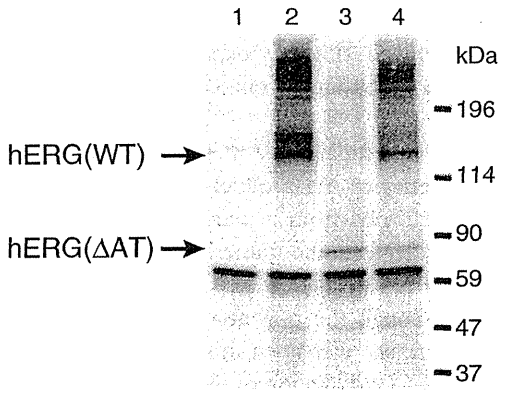

Fig. 4 Western blot analysis of hERG(WT) and hERG(ΔAT). Extracts of HEK-293 T cells were transfected with pCAGGS vector (*lane 1*), *hERG*(WT) expression vector (*lane 2*), *hERG*(ΔAT) expression vector (*lane 3*), and both *hERG*(WT) and *hERG*(ΔAT) (*lane 4*) underwent Western blot analysis using an anti-hERG antibody. The *arrows on the left* indicate the locations of the hERG(WT) and hERG(ΔAT) proteins; the positions of protein size markers are indicated on the *right side*

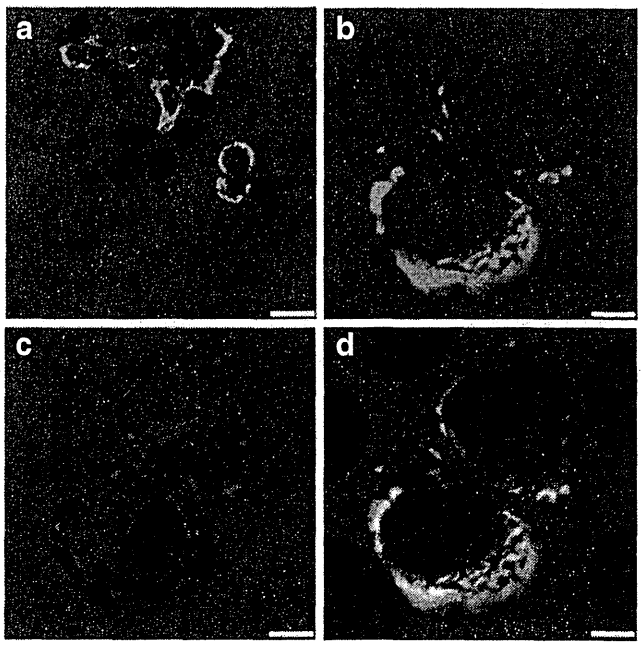

Fig. 5 Immunolabeling of HEK-293 T cells transiently transfected with HA-tagged *hERG*(WT) and Myc-tagged *hERG*(ΔAT). The immunofluorescence signals due to anti-HA antibody (*green* in **a**, **b**, and **d**) and anti-Myc antibody (*magenta* in **a**, **c**, and **d**) were merged with that from 4′,6-diamidino-2-phenylindole (*blue* in **a** and **d**). Scale bars= 25 μm (**a**) and 5 μm (**b**–**d**)